Defence Research and Development Canada
Recherche et développement pour la défense Canada

DRDC | RDDC

Theory, design, and measurement of novel uniform circular antenna arrays for direction of arrival estimation

Brad Jackson
Bruce Liao
Sreeaman Rajan
DRDC – Ottawa Research Centre

Sichun Wang
Communications Research Centre Canada

Defence Research and Development Canada

Scientific Report
DRDC-RDDC-2015-R010
January 2015

Canada

Theory, design, and measurement of novel uniform circular antenna arrays for direction of arrival estimation

Brad Jackson
Bruce Liao
Sreeaman Rajan
DRDC – Ottawa Research Centre

Sichun Wang
Communications Research Centre Canada

Defence Research and Development Canada
Scientific Report
DRDC-RDDC-2015-R010
January 2015

Abstract

The theory, design, fabrication, and measurement of new uniform circular arrays (UCAs) for direction of arrival (DOA) estimation is presented in this report. In particular, the effect of directional antenna elements in UCAs for DOA estimation is studied in detail. While the vast majority of previous work assumes isotropic antenna elements or omnidirectional dipoles, this work demonstrates that improved DOA estimation accuracy and increased bandwidth is achievable with appropriately-designed directional antennas. Simulation results in this report show improved DOA estimation accuracy and robustness using microstrip patch antennas as opposed to conventional dipoles. Additionally, it is shown that the bandwidth of a UCA for DOA estimation is limited only by the broadband characteristics of the directional antenna elements and not the electrical size of the array as is the case with omnidirectional antennas. Three novel UCAs were fabricated and tested: (1) a dipole UCA with integrated microstrip tapered baluns; (2) a narrow-spacing microstrip patch UCA; and (3) a wide-spacing microstrip patch UCA. Practical design aspects of all three arrays is detailed in this report and measurement results from an anechoic chamber are presented. This work shows that there are opportunities to improve direction finding performance through optimization of antenna array elements which could potentially improve Canadian Armed Forces direction finding and situational awareness capabilities.

Significance for defence and security

Direction finding (DF), also known as direction of arrival (DOA) estimation or angle of arrival (AOA) estimation, is a critical capability for the Canadian Armed Forces (CAF). The ability to accurately determine a line of bearing (LOB) toward an adversary's radio frequency (RF) emitter can provide vital situational awareness. In order to estimate the direction to an RF transmitter, an antenna array is generally used, which often consists of multiple identical individual antennas arranged in a uniform pattern. It is perhaps surprising that, although DF capabilities have existed for over a century, there is very little literature available on the optimization of antenna elements to improve the overall DF performance of an array.

At Defence Research & Development Canada (DRDC) – Ottawa Research Centre there has been an effort to optimize DF estimation accuracy through the use of non-traditional antenna elements. This report details new theory, simulations, and measurements that show the potential for improved DF accuracy through the use of directive antennas in uniform circular arrays (UCAs), as opposed to omnidirectional elements such as dipoles or monopoles. Improved DF performance would result in enhanced situational awareness on the battlefield for the CAF.

Résumé

Le présent rapport traite de la théorie, de la conception, de la fabrication et du mesurage de nouveaux réseaux circulaires uniformes (RCU) servant à estimer la direction du point d'origine. Nous nous penchons, plus particulièrement, sur l'effet des éléments d'antennes directives sur l'estimation de la direction du point d'origine. La grande majorité des travaux antérieurs reposent sur des éléments d'antennes isotropes ou d'antennes doublets omnidirectionnelles, mais les travaux décrits dans le présent rapport démontrent qu'il est possible d'obtenir une estimation de la direction du point d'origine plus exacte et une plus grande largeur de bande à l'aide d'antennes directives conçues de manière adéquate. De même, les résultats des simulations présentés dans le rapport montrent que l'utilisation d'antennes à plaques en microrubans assure une estimation de la direction du point d'origine plus exacte et une meilleure robustesse, par rapport aux antennes doublets classiques. Le rapport montre également que la largeur de bande d'un RCU pour l'estimation de la direction du point d'origine n'est limitée que par les caractéristiques de la large bande des éléments d'antennes directives. La taille électrique du réseau n'a aucune incidence, contrairement aux antennes omnidirectionnelles. Nous avons conçus et mis à l'essai trois nouveaux RCU : 1) un à antennes doublets muni de symétriseurs coniques en microrubans intégrés, 2) un à plaques en microrubans rapprochés et 3) un à plaques en microrubans espacés. Le rapport comporte des détails sur les aspects pratiques des trois réseaux, de même que les résultats des mesures prises en chambre anéchoïque. Les travaux montrent qu'il serait possible d'améliorer le rendement de radiogoniométrie (DF) en optimisant les éléments de réseaux d'antennes, ce qui pourrait augmenter les capacités de connaissance de la situation et de radiogoniométrie des Forces armées canadiennes (FAC).

Importance pour la défense et la sécurité

La radiogoniométrie, que l'on appelle également l'estimation de la direction du point d'origine ou de l'angle d'arrivée, est essentielle aux FAC. En effet, la capacité à déterminer exactement une ligne de relèvement vers l'émetteur radioélectrique (RF) d'un ennemi peut fournir une connaissance de la situation vitale. En règle générale, on estime la direction vers un émetteur RF à l'aide d'un réseau antennes, lequel est souvent composé de multiples antennes individuelles identiques disposées selon un diagramme uniforme. Fait étonnant : malgré la longue existence des capacités de DF (plus de 100 ans), il n'existe que très peu d'études disponibles sur l'optimisation d'éléments d'antennes en vue d'améliorer le rendement de DF global d'un réseau.

Au centre de recherches d'Ottawa de Recherche et développement pour la défense Canada (RDDC), on travaille à optimiser l'exactitude de l'estimation de DF à l'aide

d'éléments d'antennes non classiques. Le rapport traite de nouvelles théories, simulations et mesures qui montrent la possibilité d'une exactitude de DF améliorée à l'aide d'antennes directives dans des RCU, plutôt qu'au moyen d'éléments omnidirectionnels, comme des antennes doublets ou unipolaires. Un meilleur rendement de DF améliorerait la connaissance de la situation des FAC sur le champ de bataille.

Acknowledgements

The authors would like to thank several people who have made this work possible. First, we would like to acknowledge Lin Baxter, the primary sponsor of the work for helping define the project and for being available to provide information on the client's requirements. We would also like to thank Prof. Antar for generously offering the use of the printed circuit board (PCB) milling machine at the Royal Military College of Canada (RMC) as well as other lab equipment. Capt. Kyle Davidson and Mr. Martin Baxter facilitated the fabrication of the 3D printed antenna mounts and we would like to thank them for their support. Finally, Dr. Stephane Legault generously offered the use of his lab's anechoic chamber which was critical to the successful completion of this work.

Table of contents

List of figures

1 Introduction

1.1 Background

The ability to determine the location of an adversary's radio frequency (RF) transmitters is a critical capability for the Canadian Armed Forces (CAF). Direction of Arrival (DOA) estimation, also known as angle-of-arrival (AOA) estimation or direction-finding (DF), has been a subject of interest for military research for over a century. However, continual technological advances in wireless communications along with widespread proliferation of wireless devices at diminishing costs has ensured that this area of research remains active, especially through the recent developments in smart antennas. At Defence Research & Development Canada (DRDC) – Ottawa Research Centre there has been an effort to optimize DF estimation accuracy through the use of non-traditional antenna elements. In this report, new theory and designs of antenna arrays are presented that are the first of their kind to be published, and that can potentially achieve improved DF performance.

1.2 Literature review

Smart antennas have been a subject of research interest for several decades, motivated initially by military applications. Over the past 10–15 years however, this topic has received widespread interest due in large part to the proliferation of mobile communications devices. Smart antennas, or adaptive arrays, have several advantages over traditional arrays including increased coverage, improved robustness to multipath, increased system capacity, and resistance to signal interception and interference. The primary features of smart antennas are the ability to determine an incoming signal's direction of arrival (DOA) and the ability to control the radiation pattern (beamforming). This report expands and extends the work in [1] (some of this paper is reproduced for background and clarity). Specifically, this report focuses on DOA estimation and the effect of the antenna element characteristics on the achievable accuracy (see [2, 3, 4, 5, 6, 7] for a sample of recent work on DOA estimation). In general, for DOA estimation, separate receiver channels (RF front-end and digitizer) are required for each antenna element, and additional receiver channels can significantly increase size, weight, power, and cost. Therefore, it is desirable to maximize performance with a minimum number of antenna elements.

The vast majority of the work on smart antennas for DOA estimation and beamforming assume either isotropic antenna elements or, equivalently, omnidirectional elements with the analysis limited to the plane where the antenna gain is equal in all directions (e.g., a $\lambda/2$ dipole oriented on the z-axis with $\theta = 90°$) [8, 9, 10, 11]. While the literature on the individual topics of directional antennas and smart antennas is vast, there is a limited number of published papers that discuss the use of directional antennas as the elements of a smart antenna array for DOA estimation.

While uniform linear arrays (ULAs) have received the majority of the attention in the literature for beamforming and DOA estimation, uniform circular arrays (UCAs) are an attractive alternative when a more uniform performance over all azimuth angles is desired. Significant work on UCAs using directional elements has been undertaken by Davies, Rahim, *et al.* for beamforming [12, 13, 14, 15] and null-steering [16, 17, 18]. Most of this work has focused on the use of directional elements to realize wideband directional patterns by using the antenna element directivity to stabilize the mode amplitude. These papers, however, do not address DOA estimation. The optimal directional elements discussed in [12, 13, 14] are applicable for broadband beamforming as opposed to DOA estimation.

Switched antenna UCAs have been used for direction finding (e.g., [19, 20]). In the case of [19], omnidirectional monopole antennas were used whereas in [20] directive patch antennas were used on the flat surfaces of a semidodecahedron. These papers do not provide insight into the optimal antenna element for DOA estimation in adaptive smart antenna arrays. DOA estimation using directive elements is discussed in [21] for conformal surfaces (e.g., on an aircraft) as opposed to UCAs. The focus of [21] is on a general methodology for using directive elements in an adaptive array for DOA estimation and not on the effect of different antenna characteristics on DOA estimation accuracy using a specific antenna array geometry.

In [22, 23], directional circular patch antennas were used in a linear array. However, in [22] the antenna array beam was steered over all possible angles and a DOA was estimated at each potential direction. With this approach, an incoming signal's DOA can only be estimated if the direction of the incoming signal is within the radiation pattern of the main beam and it may not be possible to estimate all DOAs simultaneously. In our work, the ability to estimate all DOAs simultaneously is maintained. In [23] the focus was on a modification to the Capon algorithm for directional antenna arrays and optimizing the antenna elements themselves was not discussed.

Circular arrays using directional elements were considered in [24, 25], however, these papers focus on developing efficient DOA algorithms and do not compare the results to a realistic dipole array implementation. Furthermore, there was no discussion of the effects of different element directivities nor were there any conclusions regarding situations where directional elements may be advantageous. The design of arrays with directive properties was discussed in [26], however, in this work directive arrays were used that achieve more accurate DOA estimates over a limited range of source locations (the antenna elements themselves were assumed to be isotropic and V-shaped arrays were used).

The Cramer-Rao Lower Bound (CRLB) is commonly used to characterize the performance of DOA estimation in antenna arrays. Performance optimization using the

CRLB has been investigated from several perspectives including array geometries [26, 27]. Recently, several closed-form CRLB equations for multi-dimensional array geometries with isotropic antennas were derived [28]. However, these studies did not investigate the CRLB of UCAs with directional antenna elements.

1.3 Scientific contributions

A search of the literature did not produce any previous work that investigates the effect of antenna element directivity on DOA estimation accuracy using UCAs. Moreover, this work is the first to provide recommendations on the optimal antenna directivity for different numbers of UCA elements and for various array radii. This report is also the first to provide an explicit derivation of the CRLB for DOA estimation using UCAs with directional antennas and is the first to compare the DOA estimation accuracy of UCAs using realizable directional antenna elements with conventional dipole antennas. This work demonstrates the potential for very broadband DOA estimation using UCAs with directional antenna elements. The results shown in this report can inform antenna array designers on how to optimize DOA estimation performance while minimizing the number of antenna elements, thus potentially reducing the size, weight, power, and cost of the system.

To verify the theory and simulations of directional elements in UCAs, three antenna arrays were designed, fabricated, and tested: one dipole UCA and two directional element UCAs. To the best of our knowledge, the dipole array is the first UCA to use microstrip tapered baluns to provide balanced feeds. This balun is compact, integrated into the array support structure, and can provide a balanced signal over a wide bandwidth. The two directional element arrays consist of the same antenna element (a microstrip patch) configured for two different array radii. To the best of our knowledge these microstrip patch arrays are the first UCAs of their kind reported in the literature. All three arrays were calibrated and tested in an anechoic chamber and their measurement results compared to simulations.

1.4 Report overview

This report provides the new theory and simulation results on directional-element UCAs in Sections 2,3, and 4 following the authors' open-literature publication in [1]. Sections 5 and 6 describe the design and fabrication of the three novel UCAs for DOA estimation and provide simulation results. Section 7 provides measurement results from testing in an anechoic chamber and these results are compared to simulations. Lastly, recommendations and future work are discussed along with the conclusion in Sections 8 and 9, respectively.

2 DOA estimation theory and assumptions

2.1 UCA smart antenna receiver model

A model of a smart antenna receiver system that can be used to describe a UCA for DOA estimation is shown in Fig. 1. In this figure, a 4-element UCA (generalized in what follows as an N-element array) with a radius r and inter-element spacing d receives D incoming plane waves $s_1, s_2, \ldots, s_D$ from directions $\phi_1, \phi_2, \ldots, \phi_D$.

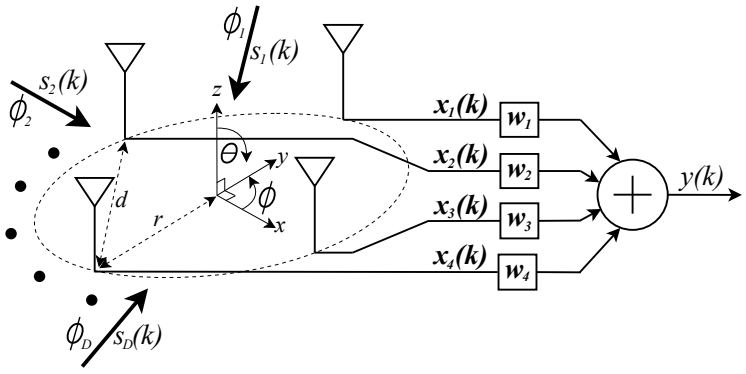

Figure 1: *UCA receiver model for DOA estimation using $N = 4$ antennas.*

It is assumed that the transmitter and receiver are stationary, and that the plane of interest coincides with the plane of the UCA (i.e., assume a 2D DOA estimation is of interest as would typically be the case for terrestrial applications). Further assume that the sensor characteristics do not vary across the bandwidth of the signals. Under these assumptions, the array output is given by:

$$y(k) = \boldsymbol{w}^H \boldsymbol{x}(k), \tag{1}$$

where k is the sample index, $[\cdot]^H$ represents the Hermitian transpose, $\boldsymbol{w}$ is a complex weight vector ($\boldsymbol{w} = [w_1\ w_2\ \ldots\ w_N]^T$), and the received signal at the antenna elements is given by:

$$\begin{aligned} \boldsymbol{x}(k) &= \begin{bmatrix} \boldsymbol{a}(\phi_1) & \boldsymbol{a}(\phi_2) & \ldots & \boldsymbol{a}(\phi_D) \end{bmatrix} \begin{bmatrix} s_1(k) \\ s_2(k) \\ \vdots \\ s_D(k) \end{bmatrix} + \boldsymbol{\eta}(k) \\ &= \boldsymbol{A} \cdot \boldsymbol{s}(k) + \boldsymbol{\eta}(k). \end{aligned} \tag{2}$$

In Eqn. (2), $\boldsymbol{a}(\phi_i)$ is the N-element array response vector (ARV) for an incoming plane wave from the direction ϕ_i, and $\boldsymbol{A}$ is an $N \times D$ matrix consisting of the D ARVs (i.e., $\boldsymbol{A}$ is the array manifold). The noise is represented by $\boldsymbol{\eta}(k)$ and is discussed in detail in the following subsection. Whereas a steering vector represents the relative phases of the received signals at the antenna elements, the ARV is a more generalized representation [29] that includes the gains of the antennas as well:

$$\boldsymbol{a}(\phi) = \begin{bmatrix} g_0(\phi)e^{j\beta p_0} \\ g_1(\phi)e^{j\beta p_1} \\ \vdots \\ g_{N-1}(\phi)e^{j\beta p_{N-1}} \end{bmatrix}, \tag{3}$$

where $\beta = 2\pi/\lambda$ is the wavenumber or phase propagation factor (λ is the signal wavelength) and $g_0(\phi), g_1(\phi), \ldots, g_{N-1}(\phi)$ are real numbers that represent the magnitude of the antenna response (i.e., the antenna gain) from the ϕ direction. For the n^{th} antenna element,

$$p_n = x_n \cos(\phi) + y_n \sin(\phi) \ , \tag{4}$$

where

$$x_n = r \cos\left(\frac{2\pi n}{N}\right) \quad \text{and} \quad y_n = r \sin\left(\frac{2\pi n}{N}\right), \quad n = 0, 1, \ldots, N-1 \ , \tag{5}$$

are the x-y Cartesian coordinates of the antenna positions (assuming $\theta = 90^\circ$ and all antennas are on the same plane, $z_n = 0$). Obviously, in the case of isotropic antennas or antennas that are omnidirectional in ϕ, $g_0 = g_1 = \ldots = g_{N-1} = 1$, which means that all DOA information is derived from the relative phase differences between the elements. In contrast, with directional elements, the DOA estimation algorithms can exploit the gain variation at different incident angles as well as phase differences to increase accuracy and robustness to ambiguous DOA estimates.

The bandwidth of a DOA system is defined in this work to be the frequency range over which the accuracy of the DOA estimates meets the desired application's requirements. This acceptable range will vary from application to application, thus in this report no absolute bandwidth figures are stated or defined, and only relative comparisons are made.

In this report it will be assumed that the N antenna elements in the UCA are identical and have a maximum gain in the direction that is radially outward from the centre of the array, $g\left(\phi - \frac{2n\pi}{N}\right)$, $n = 0, 1, \ldots, N-1$. For this case, the ARV is given by:

$$\boldsymbol{a}(\phi) = \begin{bmatrix} g\left(\phi\right) e^{j\beta r\cos\phi} \\ g\left(\phi - \frac{2\pi}{N}\right) e^{j\beta r\cos\left(\phi - \frac{2\pi}{N}\right)} \\ g\left(\phi - \frac{4\pi}{N}\right) e^{j\beta r\cos\left(\phi - \frac{4\pi}{N}\right)} \\ \vdots \\ g\left(\phi - \frac{2(N-1)\pi}{N}\right) e^{j\beta r\cos\left(\phi - \frac{2(N-1)\pi}{N}\right)} \end{bmatrix}, \tag{6}$$

where the gain $g(\cdot)$ is a non-negative smooth periodic function with period 2π.

It should be noted that since the ARV represents the magnitude and phase response of the antennas in the array from various incident angles, the gain, g, is a voltage (or current) gain relative to what would be received by a hypothetical isotropic antenna. Antennas are usually specified in terms of their radiated (or received) power in a particular direction with respect to an isotropic antenna. If an antenna's power pattern is represented by a linear gain $G(\phi)$ relative to an isotropic antenna, then $g(\phi) = \sqrt{G(\phi)}$.

2.2 Noise assumptions

The noise in the received signal $\boldsymbol{x}(k)$ is represented by $\boldsymbol{\eta}(k)$. There are several noise sources that can corrupt the received signals such as receiver noise generated by the RF front-end components including the antenna itself, noise that is "sensed" by the antennas from the environment (e.g., from galactic radiation or the sun), and noise on the signal from non-idealities in the transmitter.

For the simulation results shown in this work, receiver noise and the sensed noise are considered and are lumped together in $\boldsymbol{\eta}(k)$ in Eqn. (2). Noise on the signal from non-ideal transmitter characteristics is not included in the model, however, its incorporation is straight-forward. The received signals may also be corrupted by multipath interference, but to avoid obfuscating the discussion, the environment is assumed to be free of multipath.

It is also assumed that the sensed noise from the environment is uniform over space and equal for all antennas since the antenna elements in the array are identical (i.e., the noise does not depend on the relative antenna orientation or gain). To generate the input signal, the noiseless antenna array response is first generated using the array's ARV for the desired incoming signal azimuth angle, and then zero-mean complex Gaussian noise is added to each sample (with equal variance corresponding to the specified SNR for all antenna elements). This uniform noise assumption is used in all signal-to-noise ratios (SNRs) that follow in this report.

2.3 DOA estimation algorithms

There are a large number of algorithms that have been proposed for DOA estimation (see [30, 31] for an overview). Two of the more popular algorithms are the Classical Beamformer (CBF) [31] and Multiple Signal Classification (MUSIC) [32], both of which rely on the array correlation matrix. These two methods will be used in this report to compare the performance of UCAs using omnidirectional elements with those using directional elements. Assuming ergodicity, the time-averaged array correlation matrix of $\boldsymbol{x}(k)$ is given by:

$$\hat{\boldsymbol{R}}_{\boldsymbol{xx}} = \frac{1}{K}\sum_{k=1}^{K}\boldsymbol{x}(k)\boldsymbol{x}^H(k), \tag{7}$$

where K is the total number of samples. The Classical Beamformer, also known as the Delay-and-Sum or Bartlett method, is given by:

$$P_{CBF}(\phi) = \boldsymbol{w}^H\boldsymbol{R}_{\boldsymbol{xx}}\boldsymbol{w} = \boldsymbol{a}^H(\phi)\boldsymbol{R}_{\boldsymbol{xx}}\boldsymbol{a}(\phi), \tag{8}$$

and it uses all degrees of freedom to point the beam in different directions to find the angle that produces the strongest response.

Perhaps the most popular DOA algorithm is MUSIC, which is a subspace method that can potentially provide higher resolution by exploiting the structure of the input data model. The MUSIC spectrum is computed by:

$$P_{MUSIC}(\phi) = \frac{1}{\boldsymbol{a}^H(\phi)\boldsymbol{E}_{\boldsymbol{N}}\boldsymbol{E}_{\boldsymbol{N}}^H\boldsymbol{a}(\phi)}, \tag{9}$$

where $\boldsymbol{E}_{\boldsymbol{N}}$ represents the noise eigenvectors of $\hat{\boldsymbol{R}}_{\boldsymbol{xx}}$. In order to determine $\boldsymbol{E}_{\boldsymbol{N}}$, it is necessary to separate the signal subspace from the noise subspace. This separation can be achieved either by using a threshold or by more advanced techniques such as [33] for more robust performance. For the simulations involving MUSIC in this work, the number of incoming signals for the MUSIC algorithm is assumed to be known.

As discussed in [32], MUSIC can be formulated to include the effect of diverse signal polarization as follows:

$$P_{MUSIC}(\phi) = \frac{1}{\Lambda_{min}\left(\begin{bmatrix}\boldsymbol{a}_x^H(\phi)\\ \boldsymbol{a}_y^H(\phi)\end{bmatrix}\boldsymbol{E}_{\boldsymbol{N}}\boldsymbol{E}_{\boldsymbol{N}}^H\left[\boldsymbol{a}_x(\phi)\ \boldsymbol{a}_y(\phi)\right]\right)}, \tag{10}$$

where $\Lambda_{min}(\cdot)$ represents the minimum eigenvalue of $(\cdot)$, and $\boldsymbol{a}_x(\phi)$ and $\boldsymbol{a}_y(\phi)$ are the ARVs for two orthogonal wavefront polarizations.

In this work, the polarization of the incoming signal is assumed to be known and matched with the antennas. For more information on the practical impact of diverse signal polarizations, see [34].

2.4 CRLB of UCAs with directional antenna elements

The CRLB determines the lower bound of the variance of an unbiased estimator and is obtained from the inverse of the Fisher Information Matrix (FIM). An estimator that achieves the CRLB is considered to be efficient and it is not possible for an unbiased algorithm to outperform the CRLB. In this work, the CRLB can be used to determine the performance limit for DOA estimation and the effect of antenna directivity on the CRLB. The CRLB will be derived in this report for the single path case; for more information on multipath CRLB, see [35]. Although we are not interested in the channel gain and phase, they must be accounted for in the CRLB derivation, and thus the signal vector for a single incident signal at any sample instant is given by:

$$\boldsymbol{x} = \alpha e^{jb}\boldsymbol{a}(\phi) + \boldsymbol{\eta} \ , \tag{11}$$

where α represents the channel and signal gain and b represents the channel and signal phase, and

$$\boldsymbol{\eta} = \begin{bmatrix} \eta_0 \\ \eta_1 \\ \vdots \\ \eta_{N-1} \end{bmatrix} \tag{12}$$

is a complex-valued zero-mean circular Gaussian random vector with

$$E(\eta_u \eta_v^*) = \sigma^2 \delta_{uv}, 0 \leq u, v \leq N-1 \ ,$$

where σ^2 represents the variance in the noise $\boldsymbol{\eta}$, and * denotes the complex conjugation operation.

The probability density $f = f(\boldsymbol{x}|\alpha, b, \phi)$ of the signal vector $\boldsymbol{x}$ defined by (11) is computed by:

$$\begin{aligned} & f(\boldsymbol{x}|\alpha, b, \phi) \\ & = c \exp\left\{ -\frac{(\boldsymbol{x} - \alpha e^{jb}\boldsymbol{a}(\phi))^H (\boldsymbol{x} - \alpha e^{jb}\boldsymbol{a}(\phi))}{\sigma^2} \right\} \ , \end{aligned} \tag{13}$$

where c is a positive constant independent of the parameters α, b and ϕ. The log-likelihood function is:

$$\begin{aligned}
&\log\left(f(\boldsymbol{x}|\alpha,b,\phi)\right)\\
&=\log(c)-\frac{(\boldsymbol{x}-\alpha e^{jb}\boldsymbol{a}(\phi))^H(\boldsymbol{x}-\alpha e^{jb}\boldsymbol{a}(\phi))}{\sigma^2}\\
&=C+\frac{1}{\sigma^2}\left[\alpha e^{-jb}\boldsymbol{a}^H(\phi)+\alpha e^{jb}\boldsymbol{x}^H\boldsymbol{a}(\phi)-\alpha^2\boldsymbol{a}^H(\phi)\boldsymbol{a}(\phi)\right]\\
&=C+\frac{1}{\sigma^2}h\ ,
\end{aligned}\tag{14}$$

where $C=\log(c)-\sigma^{-2}\boldsymbol{x}^H\boldsymbol{x}$, and

$$h=\alpha e^{-jb}\boldsymbol{a}^H(\phi)\boldsymbol{x}+\alpha e^{jb}\boldsymbol{x}^H\boldsymbol{a}(\phi)-\alpha^2\boldsymbol{a}^H(\phi)\boldsymbol{a}(\phi).$$

The Fisher Information Matrix, denoted by F, is computed by:

$$F=-\frac{1}{\sigma^2}\begin{bmatrix} E\left(\frac{\partial^2 h}{\partial\alpha^2}\right) & E\left(\frac{\partial^2 h}{\partial\alpha\partial b}\right) & E\left(\frac{\partial^2 h}{\partial\alpha\partial\phi}\right)\\ E\left(\frac{\partial^2 h}{\partial b\partial\alpha}\right) & E\left(\frac{\partial^2 h}{\partial b^2}\right) & E\left(\frac{\partial^2 h}{\partial b\partial\phi}\right)\\ E\left(\frac{\partial^2 h}{\partial\phi\partial\alpha}\right) & E\left(\frac{\partial^2 h}{\partial\phi\partial b}\right) & E\left(\frac{\partial^2 h}{\partial\phi^2}\right)\end{bmatrix}.\tag{15}$$

It can be verified that

$$\frac{\partial h}{\partial\alpha}=e^{-jb}\boldsymbol{a}^H(\phi)\boldsymbol{x}+e^{jb}\boldsymbol{x}^H\boldsymbol{a}(\phi)-2\alpha\boldsymbol{a}^H(\phi)\boldsymbol{a}(\phi)\ ,\tag{16}$$

$$\frac{\partial h}{\partial b}=-\alpha j e^{-jb}\boldsymbol{a}^H(\phi)\boldsymbol{x}+\alpha j e^{jb}\boldsymbol{x}^H\boldsymbol{a}(\phi)\ ,\tag{17}$$

$$\frac{\partial h}{\partial\phi}=\alpha e^{-jb}\left(\frac{\partial\boldsymbol{a}}{\partial\phi}\right)^H\boldsymbol{x}+\alpha e^{jb}\boldsymbol{x}^H\frac{\partial\boldsymbol{a}}{\partial\phi}-\alpha^2\left[\left(\frac{\partial\boldsymbol{a}}{\partial\phi}\right)^H\boldsymbol{a}(\phi)+\boldsymbol{a}^H(\phi)\frac{\partial\boldsymbol{a}}{\partial\phi}\right]\ ,\tag{18}$$

$$\frac{\partial^2 h}{\partial\alpha^2}=-2\boldsymbol{a}^H(\phi)\boldsymbol{a}(\phi)\ ,\tag{19}$$

$$\frac{\partial^2 h}{\partial\alpha\partial b}=-je^{-jb}\boldsymbol{a}^H(\phi)\boldsymbol{x}+je^{jb}\boldsymbol{x}^H\boldsymbol{a}(\phi)\ ,\tag{20}$$

$$\frac{\partial^2 h}{\partial\alpha\partial\phi}=e^{-jb}\left(\frac{\partial\boldsymbol{a}}{\partial\phi}\right)^H\boldsymbol{x}+e^{jb}\boldsymbol{x}^H\frac{\partial\boldsymbol{a}}{\partial\phi}-2\alpha\left(\frac{\partial\boldsymbol{a}}{\partial\phi}\right)^H\boldsymbol{a}(\phi)-2\alpha\boldsymbol{a}^H(\phi)\frac{\partial\boldsymbol{a}}{\partial\phi}\ ,\tag{21}$$

$$\frac{\partial^2 h}{\partial b \partial \alpha} = \frac{\partial^2 h}{\partial \alpha \partial b} \, , \tag{22}$$

$$\frac{\partial^2 h}{\partial b^2} = -\alpha e^{-jb} \boldsymbol{a}^H(\phi)\boldsymbol{x} - \alpha e^{jb} \boldsymbol{x}^H \boldsymbol{a}(\phi) \, , \tag{23}$$

$$\frac{\partial^2 h}{\partial b \partial \phi} = -\alpha j e^{-jb} \left(\frac{\partial \boldsymbol{a}}{\partial \phi} \right)^H \boldsymbol{x} + \alpha j e^{jb} \boldsymbol{x}^H \frac{\partial \boldsymbol{a}}{\partial \phi} \, , \tag{24}$$

$$\frac{\partial^2 h}{\partial \phi \partial \alpha} = \frac{\partial^2 h}{\partial \alpha \partial \phi} \, , \tag{25}$$

$$\frac{\partial^2 h}{\partial \phi \partial b} = \frac{\partial^2 h}{\partial b \partial \phi} \, , \tag{26}$$

$$\begin{aligned} \frac{\partial^2 h}{\partial \phi^2} &= \alpha e^{-jb} \left(\frac{\partial^2 \boldsymbol{a}}{\partial \phi^2} \right)^H \boldsymbol{x} + \alpha e^{jb} \boldsymbol{x}^H \frac{\partial^2 \boldsymbol{a}}{\partial \phi^2} \\ &- \alpha^2 \left[\left(\frac{\partial^2 \boldsymbol{a}}{\partial \phi^2} \right)^H \boldsymbol{a}(\phi) + 2 \left(\frac{\partial \boldsymbol{a}}{\partial \phi} \right)^H \frac{\partial \boldsymbol{a}}{\partial \phi} + \boldsymbol{a}^H(\phi) \frac{\partial^2 \boldsymbol{a}}{\partial \phi^2} \right] . \end{aligned} \tag{27}$$

Applying the basic fact that

$$E(\boldsymbol{x}) = \alpha e^{jb} \boldsymbol{a}(\phi), \quad E(\boldsymbol{x}^H) = \alpha e^{-jb} \boldsymbol{a}^H(\phi), \tag{28}$$

the following identities hold:

$$E\left(\frac{\partial^2 h}{\partial \alpha^2} \right) = -2\boldsymbol{a}^H(\phi)\boldsymbol{a}(\phi) = -2 \left\| \boldsymbol{a}(\phi) \right\|^2 \, , \tag{29}$$

$$E\left(\frac{\partial^2 h}{\partial \alpha \partial b} \right) = 0 \, , \tag{30}$$

$$E\left(\frac{\partial^2 h}{\partial \alpha \partial \phi} \right) = -\alpha \frac{\partial}{\partial \phi} \left(\left\| \boldsymbol{a}(\phi) \right\|^2 \right) \, , \tag{31}$$

$$E\left(\frac{\partial^2 h}{\partial b^2} \right) = -2\alpha^2 \boldsymbol{a}^H(\phi)\boldsymbol{a}(\phi) = -2\alpha^2 \left\| \boldsymbol{a}(\phi) \right\|^2 \, , \tag{32}$$

$$E\left(\frac{\partial^2 h}{\partial b \partial \phi}\right) = -\alpha^2 j \left[\left(\frac{\partial \boldsymbol{a}}{\partial \phi}\right)^H \boldsymbol{a}(\phi) - \boldsymbol{a}^H(\phi)\frac{\partial \boldsymbol{a}}{\partial \phi}\right] , \tag{33}$$

$$E\left(\frac{\partial^2 h}{\partial \phi^2}\right) = -2\alpha^2 \left\|\frac{\partial \boldsymbol{a}}{\partial \phi}\right\|^2 . \tag{34}$$

In summary, the elements of the FIM are given by:

$$\begin{cases} E\left(\frac{\partial^2 h}{\partial \alpha^2}\right) &= -2\left\|\boldsymbol{a}(\phi)\right\|^2 \\ E\left(\frac{\partial^2 h}{\partial \alpha \partial b}\right) &= 0 \\ E\left(\frac{\partial^2 h}{\partial \alpha \partial \phi}\right) &= -\alpha \frac{\partial}{\partial \phi}\left(\left\|\boldsymbol{a}(\phi)\right\|^2\right) \\ E\left(\frac{\partial^2 h}{\partial b \partial \alpha}\right) &= E\left(\frac{\partial^2 h}{\partial \alpha \partial \phi}\right) = 0 \\ E\left(\frac{\partial^2 h}{\partial b^2}\right) &= -2\alpha^2\left\|\boldsymbol{a}(\phi)\right\|^2 \\ E\left(\frac{\partial^2 h}{\partial b \partial \phi}\right) &= -\alpha^2 j\left[\left(\frac{\partial \boldsymbol{a}}{\partial \phi}\right)^H \boldsymbol{a}(\phi) - \boldsymbol{a}(\phi)^H \frac{\partial \boldsymbol{a}}{\partial \phi}\right] \\ E\left(\frac{\partial^2 h}{\partial \phi \partial \alpha}\right) &= E\left(\frac{\partial^2 h}{\partial \alpha \partial \phi}\right) \\ E\left(\frac{\partial^2 h}{\partial \phi \partial b}\right) &= E\left(\frac{\partial^2 h}{\partial b \partial \phi}\right) \\ E\left(\frac{\partial^2 h}{\partial \phi^2}\right) &= -2\alpha^2\left\|\frac{\partial \boldsymbol{a}}{\partial \phi}\right\|^2 \end{cases} , \tag{35}$$

where $||\cdot||$ represents the second norm.

It can be verified that

$$\left\|\boldsymbol{a}(\phi)\right\|^2 = \sum_{n=0}^{N-1}\left(g\left(\phi - \frac{2\pi n}{N}\right)\right)^2 , \tag{36}$$

$$\frac{\partial}{\partial \phi}\left\|\boldsymbol{a}(\phi)\right\|^2 = 2\sum_{n=0}^{N-1} g\left(\phi - \frac{2\pi n}{N}\right) g'\left(\phi - \frac{2\pi n}{N}\right) , \tag{37}$$

$$\left\|\frac{\partial \boldsymbol{a}}{\partial \phi}\right\|^2 = \sum_{n=0}^{N-1}\left(g'\left(\phi - \frac{2\pi n}{N}\right)\right)^2 + \sum_{n=0}^{N-1}\beta^2 r^2\left(g\left(\phi - \frac{2\pi n}{N}\right)\right)^2 \sin^2\left(\phi - \frac{2\pi n}{N}\right) , \tag{38}$$

$$\alpha^2 j\left[\left(\frac{\partial \boldsymbol{a}}{\partial \phi}\right)^H \boldsymbol{a}(\phi) - \boldsymbol{a}^H \frac{\partial \boldsymbol{a}}{\partial \phi}\right] = -2\alpha^2\beta r\sum_{n=0}^{N-1}\left(g\left(\phi - \frac{2\pi n}{N}\right)\right)^2 \sin\left(\phi - \frac{2\pi n}{N}\right) , \tag{39}$$

where $g'(\cdot)$ represents the first derivative of the antenna gain with respect to ϕ.

If the inverse of the Fisher Information Matrix is given by $J = F^{-1}$, then the CRLB for a particular azimuth angle is given by:

$$CRLB(\phi) = J_{33} = \frac{2\sigma^2\alpha^{-2}\|\boldsymbol{a}(\phi)\|^2}{\Delta} \,, \tag{40}$$

where

$$\Delta = 4\|\boldsymbol{a}(\phi)\|^2 \left\|\frac{\partial \boldsymbol{a}}{\partial \phi}\right\|^2 + \left|\left(\frac{\partial \boldsymbol{a}}{\partial \phi}\right)^H \boldsymbol{a}(\phi) - a^H \frac{\partial \boldsymbol{a}}{\partial \phi}\right|^2 - \left|\frac{\partial}{\partial \phi}\left(\|\boldsymbol{a}(\phi)\|^2\right)\right|^2 . \tag{41}$$

For the isotropic case, $g(\phi) = 1$ and $g'(\phi) = 0$ for all ϕ and the CRLB simplifies to the UCA CRLB formula presented elsewhere (e.g., see [36]).

The formula presented in Eqn. (40) can be used to determine the optimal directivity or radiation pattern for a particular number of antenna elements and UCA radius. Given the practical possibilities for far-field gain patterns of potential antenna elements, the set of gain functions $g(\cdot)$ may be restricted and could result in further simplifications to the CRLB. Standard optimization procedures could be used to determine the overall optimum array design that minimizes DOA estimation error by finding the parameters that minimize the CRLB.

2.5 UCA phase ambiguities

While the CRLB derived in the previous subsection can provide insight into the performance limit using an unbiased DOA estimator, it does not provide information on potential phase ambiguities. In arrays where isotropic or omnidirectional elements are assumed, the DOA information is derived entirely from the phase response of the antennas in the array, which in turn is determined by the element positions. In ULAs, the element spacing is generally kept to less than $\lambda/2$ to avoid grating lobes and potential ambiguities in DOA estimation. With UCAs, the problem of phase ambiguities can be avoided as long as a sufficient number of elements is chosen. However, in many cases, it is desirable to use a minimal number of channels to achieve low cost, size, and complexity.

In the particular case of a 4-element UCA using isotropic elements, the first ambiguity occurs for an array radius of $r = \lambda/(2\sqrt{2})$. At this radius, the inter-element spacing $d = \lambda/2$ and phase ambiguities occur for incoming signals arriving at odd-integer multiples of 45° since at these angles the phase difference between pairs of antennas is 180°. UCAs with radius less than $r = \lambda/(2\sqrt{2})$ will not have any phase ambiguities and those with larger array radius will have an increasing number of potential ambiguities as the radius increases.

Although phase ambiguities can occur with 4-element UCAs with a radius of $r = \lambda/(2\sqrt{2})$ or greater, these can potentially be resolved by using the antenna gain information, assuming the antennas have different gains in the directions of the potential ambiguous incident signals (e.g., with directive antennas or through the effects of mounting omnidirectional antennas on a vehicle). This is in contrast to other techniques such as [37] where ambiguity resolution is achieved through modifying the array geometry. The ability to use the gain variation of the antenna elements to resolve phase ambiguities could potentially result in an increased DOA system bandwidth since the maximum electrical size of the array would not be fundamentally limited.

3 DOA estimation with theoretical directional UCA elements

3.1 Antenna gain pattern synthesis

In order to investigate the effect of a directional pattern on the DOA accuracy both in the CRLB as well as through simulations, a model for the radiation pattern of hypothetical antenna elements must be known. At this point, practical antenna design issues and constraints are not considered; rather, the goal is to select a mathematical representation of an antenna's radiation pattern and investigate the effect of directivity on DOA estimation accuracy. The antenna element far-field power pattern model that is the focus of this section has a $(1+\cos(\phi))^m$ response in the plane of interest, where m controls the directivity. This pattern has increasing directivity as m increases and has maximum gain at $\phi = 0°$. Rather than have no back-side radiation, the proposed pattern can provide a closer approximation to antennas that exhibit back-side radiation such as microstrip patches with finite substrates. Assuming a symmetrical 3D pattern, the proposed theoretical normalized radiation patterns for the N antennas in the UCA are given by:

$$U_n(\theta,\phi) = \tfrac{1}{2^{2m}}\left(1+\sin(\theta)\right)^m \left(1+\cos\left(\phi - \tfrac{2\pi n}{N}\right)\right)^m \\ n = 0, 1, \ldots, N-1. \tag{42}$$

Note that the maximum directivity of each element is in a direction that points radially outward from the centre of the array, evenly spaced around the UCA.

With the proposed mathematical radiation pattern given in Eqn. (42), the directivity of each identical antenna element in the array is given by [38]:

$$D = \frac{2^{2m+2}\pi}{\int_0^{2\pi}\int_0^{\pi}(1+\sin(\theta))^m(1+\cos(\phi)))^m \sin\theta d\theta d\phi}. \tag{43}$$

For the isotropic case, $m = 0$ and $D = 1$ in Eqn. (43), and as m increases, the directivity, D, increases. For example, when $m \approx 2.7$, $D = 4$, and when $m \approx 8.7$, the directivity is $D = 10$.

From Eqn. (42), with the assumption that the antennas are perfectly matched and lossless, the theoretical model of the antenna's far-field power patterns in the $\theta = 90°$ plane relative to an isotropic antenna are given by:

$$G(\phi) = \frac{D}{2^m}\left(1+\cos\left(\phi - \frac{2\pi n}{N}\right)\right)^m, \; n = 0, 1, \ldots, N-1. \tag{44}$$

Shown in Fig. 2 are the radiation patterns of the hypothetical antenna elements for $\theta = 90°$, as described by Eqn. (44) with directivities of $D = 2, 4, 10, 25, 50$ (3 dBi to 17 dBi) as well as an isotropic pattern (0 dBi) for reference.

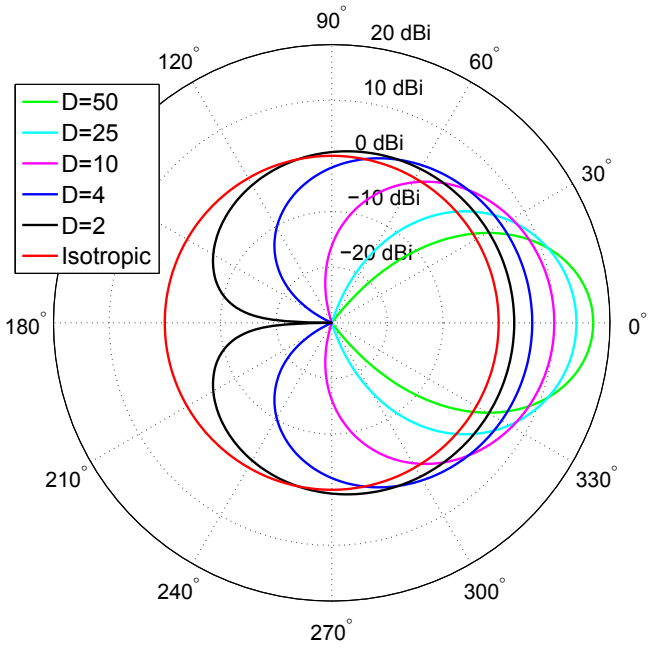

Figure 2: *Directional power patterns from Eqn. (44) for various values of directivity, $D = 1, 2, 4, 10, 25, 50$ (0 dBi to 17 dBi), $\theta = 90°$.*

3.2 CRLB performance

With the antenna gain pattern known, the CRLB can be computed using the formulation in Section 2.4. Shown in Fig. 3 is the average CRLB for UCA radii of $r = \lambda/10$, $r = \lambda/4$, and $r = \lambda$. Whereas in UCAs with isotropic antennas the CRLB is constant for all azimuth angles, ϕ, with directive antennas the CRLB varies depending on ϕ. With $N = 4$ antennas with the gain patterns discussed in the previous section, the CRLB is periodic, and repeats every $\pi/4$. Note that the dependence of the CRLB on ϕ is also exhibited in ULAs with isotropic elements (e.g., see [36]). For each UCA radius, r, and for each value of directivity, the average CRLB was computed by taking the mean of the CRLB over the full 360° of ϕ. Since the CRLB varies with ϕ for directional antennas, it is possible that the CRLB could exceed the isotropic CRLB for some ϕ while maintaining an average that is less than this value. The shaded areas in Fig. 3 represent the bounds of the CRLB as it varies over ϕ for a particular value of r and D. For example, when $r = \lambda/10$, the CRLB for a directivity of $D = 3$ will vary between values of 0.1 and 0.12 with an average value of 0.11. The

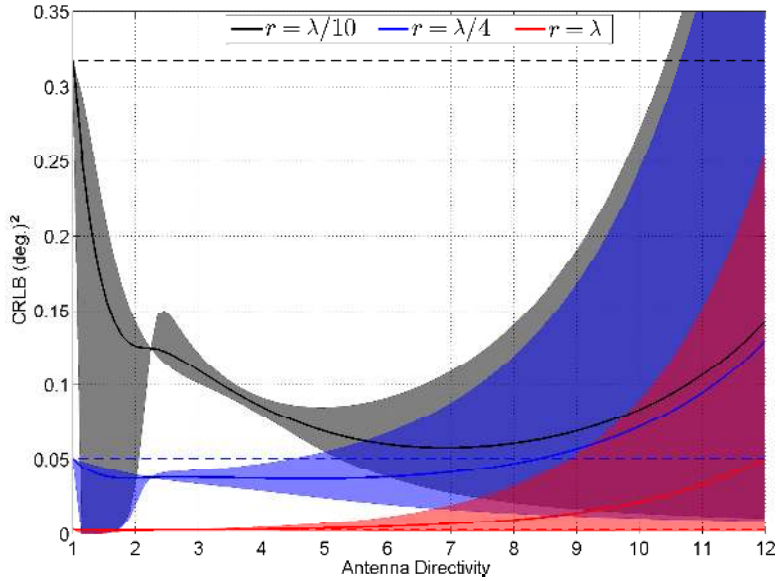

Figure 3: *CRLB for a 4-element UCA with various radii with an SNR of 0 dB. The shaded areas show the range of variation in the CRLB over ϕ for a particular value of r and D.*

variation in CRLB depends on the directivity, and interestingly, is almost constant at approximately $D = 2.25$. If uniform performance is desired across ϕ then the antenna elements can be designed to have this value of directivity. If, however, some variation in CRLB over ϕ is acceptable then lower average errors can potentially be achieved at higher directivities. At large values of directivity the limited coverage of the antenna radiation patterns causes large errors at some angles that greatly exceed the isotropic CRLB.

It is apparent from Fig. 3 that there is the potential for improved performance through the use of directional antennas. For the case of $r = \lambda/10$, there is over a 6 dB improvement in the average CRLB for values of directivity between $D = 4$ and $D = 10$ (between 6 dBi and 10 dBi) compared to the isotropic CRLB (illustrated with a dashed line in Fig. 3 corresponding to the color used for the particular array radius, r). As mentioned previously, a 4-element UCA with isotropic elements can produce ambiguous results when $r \geq \lambda/(2\sqrt{2})$. The CRLB formulation does not include information regarding the potential ambiguities present in the array configuration and therefore shows a monotonically decreasing average CRLB as the radius of the array increases even for isotropic antennas with array radii greater than $\lambda/(2\sqrt{2})$, which is not a realizable result in practice. In contrast, it will be shown through simulations that the use of directive antennas resolves the phase ambiguities present with isotropic antennas. The general trend in the CRLB from Fig. 3 is that the antenna directivity that results in the minimum CRLB decreases as the array radius

increases. For instance, the minimum average CRLB occurs at approximately $D = 7$ for $r = \lambda/10$, $D = 5$ for $r = \lambda/4$, and $D = 2$ for $r = \lambda$. For a 4-element UCA, a directivity in the range of 2 to 5 can produce good performance over a two decade change in array radius, or equivalently, over a two decade bandwidth.

The average CRLB performance for $N = 8$ is shown in Fig. 4 for $r = \lambda/4$, $r = \lambda/2$, and $r = \lambda$ with an SNR of -10 dB. Similar to the $N = 4$ case a better CRLB is achieved compared to the isotropic case by using directive antennas. Note that the directivities that produce the minimum average CRLB have increased relative to the $N = 4$ case and that similar behavior is displayed with large maximum CRLBs for high values of directivity.

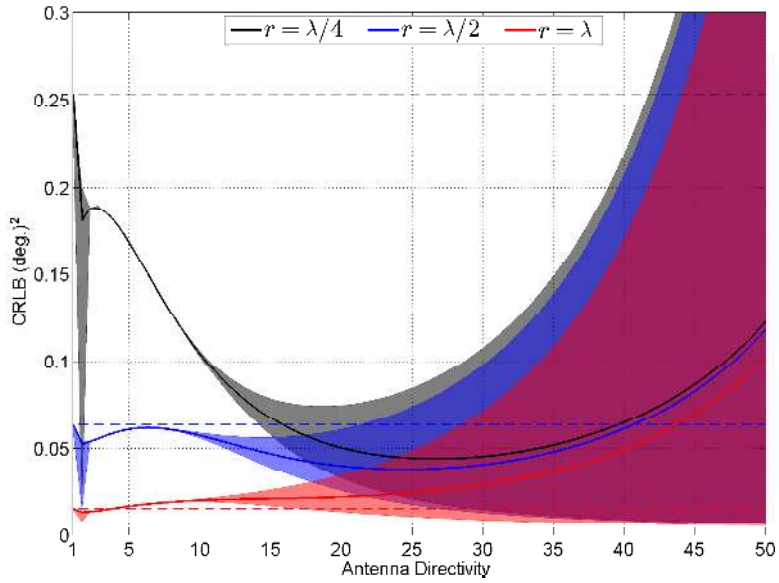

Figure 4: *CRLB for an 8-element UCA with various radii with an SNR of* -10 *dB.The shaded areas show the range of variation in the CRLB over* ϕ *for a particular value of* r *and* D*.*

3.3 Simulation results

Simulations were performed to confirm the CRLB results and to determine the directivity that generates the lowest DOA estimation error using the patterns described by Eqn. (44) for a common DOA estimation algorithm (MUSIC). Unless otherwise noted, all simulations in this report use a single sinusoidal incident plane wave with $K = 100$ snapshots or samples (i.e., $k = 0, 1, \ldots, 99$). In simulations where the incident signal direction ϕ_i was swept, the increment was 1° and for each incident signal angle, $L = 1000$ runs were performed. The DOA estimation root mean square error

(RMSE) for an incident angle ϕ_i is defined by:

$$\text{RMSE} = \sqrt{\left(\frac{1}{IL}\sum_{i=0}^{I-1}\sum_{l=0}^{L-1}(\hat{\phi}_{i,l} - \phi_i)^2\right)} \quad , \tag{45}$$

where $\hat{\phi}_{i,l}$ is the estimated DOA for ϕ_i with $I = 360$. It has been shown [39] that the MUSIC algorithm approaches the CRLB as the number of samples $k \to \infty$, and it will be seen through the following simulation results that even with a limited number of samples the CRLB can predict the relative performance of UCAs with different antenna directivities.

Shown in Fig. 5 are the DOA errors for different antenna elements at various UCA radii for a SNR of 0 dB over the full 360° range of possible incoming azimuth signals as described above for $N = 4$ antenna elements. As discussed in Section 2.5, for the isotropic case, ambiguities occur for 4-element UCAs for $r \geq \lambda/(2\sqrt{2})$, which is the reason for the sharp increase in DOA estimation error at radii above this value. Clearly, the range of array radii is very limited for isotropic antennas compared to antennas with a directivity in the range of $D = 2$ to $D = 10$, and even at radii where there are no ambiguities with isotropic antennas, the accuracy can still be improved with directive antennas.

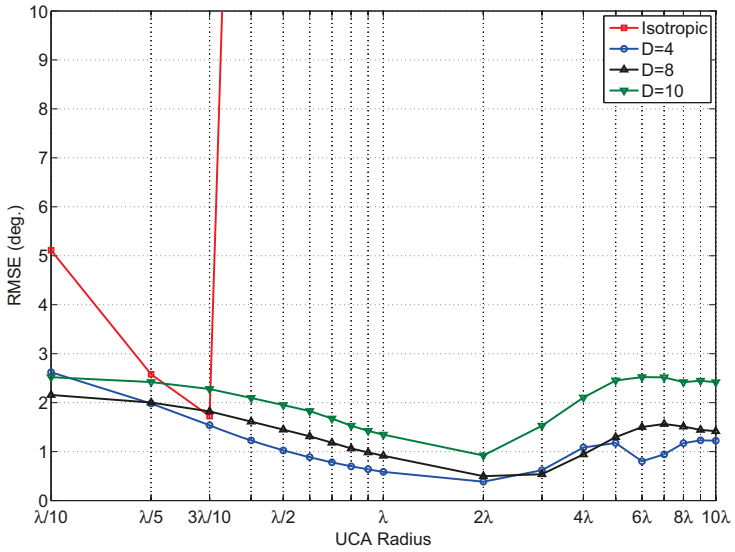

Figure 5: *DOA estimation RMSE using the MUSIC algorithm for a 4-element UCA with various radii with an SNR of 0 dB (logarithmic x-axis).*

Considering the trends in Fig. 3 and Fig. 5, it is clear that the CRLB is useful for predicting the relative performance for different antenna directivities. For example, with $r = \lambda/10$, the CRLB in Fig. 3 predicts that the isotropic antennas will have the

poorest performance, followed by $D = 2$, $D = 4$, and $D = 8$ having the lowest average error. As another example, it would be predicted from Fig. 3 that with a UCA radius of $r = \lambda$ that the poorest performance (other than the isotropic antenna which, as discussed, has phase ambiguities above $r = \lambda/(2\sqrt{2})$) would be with a directivity of $D = 10$, followed by $D = 8$ and the best performance would result from directivities of $D = 2$ and $D = 4$. From the $r = \lambda$ points in Fig. 5, it can be seen that it follows the trend seen in the CRLB plot in Fig. 3. Similarly, for other values of array radii the CRLB can be used to generally predict the performance. A directivity in the range of $D = 2$ to $D = 5$ appears to be a reasonable compromise for DOA estimation performance across a range of array radii. Note that with the directivities shown in Fig. 5 that sub-3° accuracy is achieved over a two-decade change in array radius or, equivalently, a two-decade frequency bandwidth, assuming the antenna elements can maintain constant characteristics over this bandwidth. Therefore, in practice, the bandwidth of the UCA would be limited by the broadband performance of the antennas themselves as opposed to the electrical size of the array.

The DOA estimation errors over possible incoming azimuth angles for an 8-element UCA is shown in Fig. 6 for an SNR of -10 dB. In this case, the directivity of the theoretical elements that results in the best DOA estimation performance over the range of array radii is $D = 25$ (14 dBi) and the general trends predicted from the CRLB in Fig. 4 are confirmed. As with the $N = 4$ case, the isotropic elements produce accurate DOA estimates over a relatively narrow array spacing range, or equivalently, over a narrow bandwidth due to phase ambiguities. Furthermore, Fig. 6 shows that directional elements outperform the omnidirectional elements regardless of array spacing. Therefore, it can be advantageous to use directional elements with appropriate directivity as opposed to isotropic, particularly in low-SNR situations such as this.

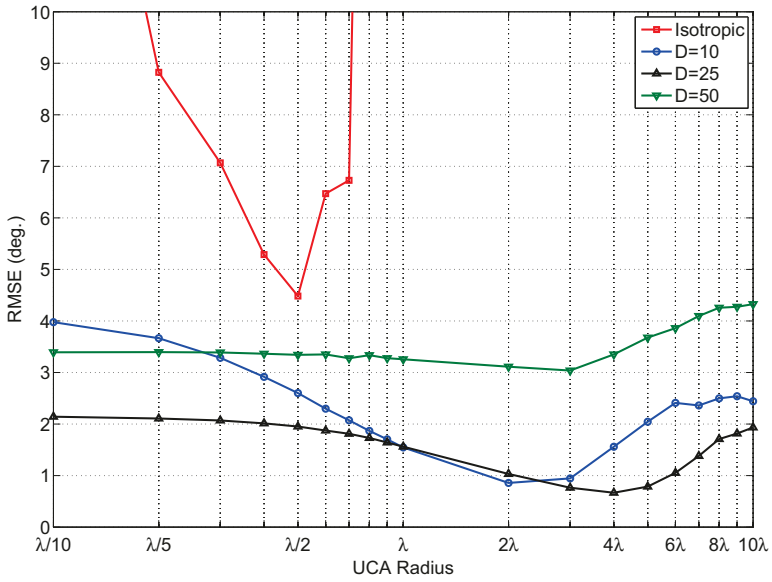

Figure 6: *DOA estimation RMSE using the MUSIC algorithm for an 8-element UCA with various radii r with an SNR of -10 dB (logarithmic x-axis).*

4 Simulated DOA estimation performance with microstrip patch and dipole antenna elements

The antenna element gain patterns explored in the previous section were mathematical models that did not consider the realities and constraints of a physical antenna design. In this section, a design that approximates the pattern found to have the lowest DOA estimation error in the previous section will be discussed and its performance will be compared to $\lambda/2$ dipole antennas for a 4-element UCA. A specific frequency of 1.0 GHz was selected and the antennas were designed and simulated using FEKO, a full wave, method of moments (MoM) based electromagnetics (EM) analysis software [40]. For the directional elements, a rectangular microstrip patch antenna was designed since these antennas are directional and typically have gains of approximately 6–9 dBi, which is close to the optimal directivity found for a 4-element UCA in Section 3 (both through the CRLB as well as in simulations). While microstrip patch antennas are typically narrow-band, this very well-known design is useful to illustrate the performance and utility of directional antennas in UCA DOA estimation. In the previous section the power pattern was described in terms of its directivity, D. In this section, since a practical antenna is being considered, the antenna's realized gain, G, will be used rather than its directivity since realized gain includes losses in the antenna as well as losses due to impedance mismatches. The antenna element was designed for a linear power gain of 4 relative to isotropic, which provided the lowest errors from the CRLB and simulations (while also maintaining a CRLB value less than the isotropic CRLB for all ϕ, see Fig. 3).

A dipole UCA with 4-elements is shown in Fig. 7(a) and a 4-element UCA using the microstrip patch directional elements is shown in Fig. 7(b). For all antennas, the load resistance is $R_L = 50\ \Omega$. With reference to Fig. 7, the length of the dipole antennas were designed to be slightly less than $\lambda/2$ in order to improve matching to the 50 Ω load through the reduction of the real and imaginary input impedance components (145.0 mm, which produced an input reflection coefficient of -15 dB at 1 GHz). The dipoles had perfect vertical orientation and ideal feeds were used. Therefore, they have no cross-polarization response and Eqn. (9) was used to estimate the DOA.

The microstrip patch antenna was designed by using an optimization algorithm where the goal was to minimize the difference between the simulated far-field radiation pattern and the theoretical pattern from Eqn. (44) with $D = 4$, while simultaneously achieving an input return loss better than -10 dB. The resulting optimized dimensions of the microstrip antenna was as follows: $W_{sub} = \lambda/2 = 150.0$ mm, $L_{sub} = \lambda/2 = 150.0$ mm, $W = 107.2$ mm, $L = 96.5$ mm, $W_{50} = 9.8$ mm, $W_{slot} = 2.4$ mm, $L_{slot} = 21.7$ mm, $t = 3.175$ mm, $\epsilon_r = 2.2$ (Rogers RT/duroid 5880 substrate). The design used a relatively small substrate ($\lambda/2 \times \lambda/2$) in order to realize arrays with radii as low as $r = \lambda/4$. The use of an inset feed ($W_{slot} \times L_{slot}$) is a common technique

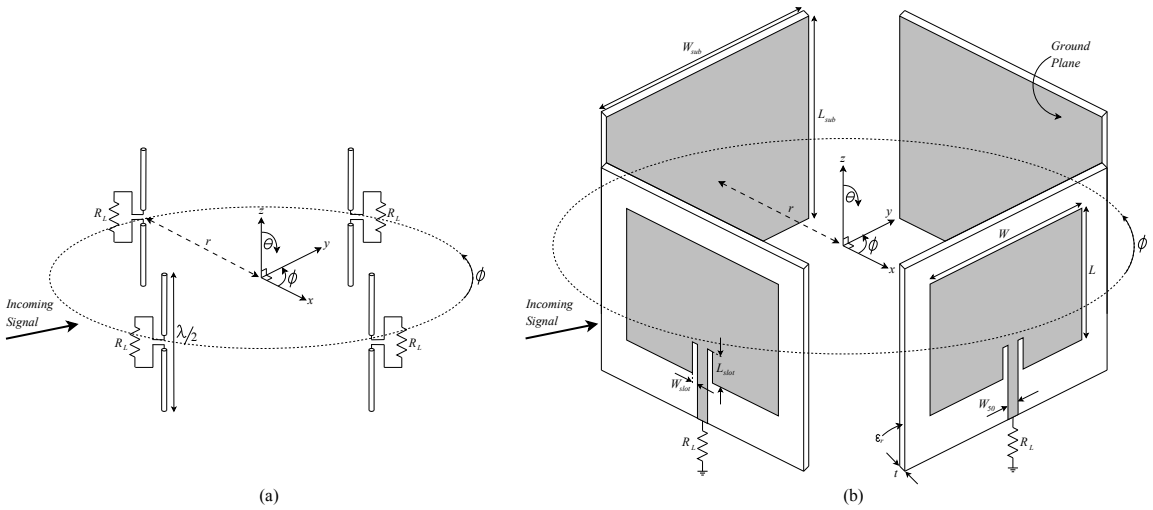

Figure 7: *(a) 4-element $\lambda/2$ dipole UCA. (b) 4-element microstrip UCA.*

to improve the input impedance match of microstrip antennas.

The radiation pattern of the theoretical directional element (Eqn. (44) with $D = 4$) is compared to the gain pattern of a microstrip patch obtained from EM simulation in Fig. 8 with the patch oriented along the z-axis and facing in the $\phi = 0°$ direction with $\theta = 90°$ as shown in Fig. 7 (i.e., the x-y or H-plane). From Fig. 8 it is clear that the microstrip patch is a reasonable approximation to the theoretical model from Eqn. (44) with $D = 4$. Also evident from the gain pattern in Fig. 8 is the backside radiation which is present since the ground plane is not infinite in extent (and in this case is relatively electrically small). The difference in peak gain between the theoretical pattern and the microstrip patch is approximately 0.7 dB. The simulated input impedance match ($|S_{11}|$) of the microstrip patch antenna in isolation was found to be -12 dB. From the co-polarization and cross-polarization microstrip patterns in Fig. 8, it is clear that the cross-polarization discrimination (XPD) is high for this antenna (between 13 dB and 46 dB for all azimuth angles). Since the XPD is high and the signal polarization is assumed to match the antennas, the DOA estimates are computed using only the co-polarization ARV for the microstrip array (i.e., Eqn. (9)).

In order to generate a calibrated ARV for both the dipole and microstrip arrays, the arrays were separately implemented in FEKO and vertically polarized incoming plane waves were generated and swept in the plane of interest ($\theta = 90°$) with 1° increments in azimuth angle, ϕ. A complete EM simulation was performed including all elements for both the dipole UCAs and microstrip UCAs at each value of array radius. As such, the effects of shadowing from the microstrip patches (Fig. 7(b)) are included in the ARV and the simulation results that follow. The magnitudes and phases of the

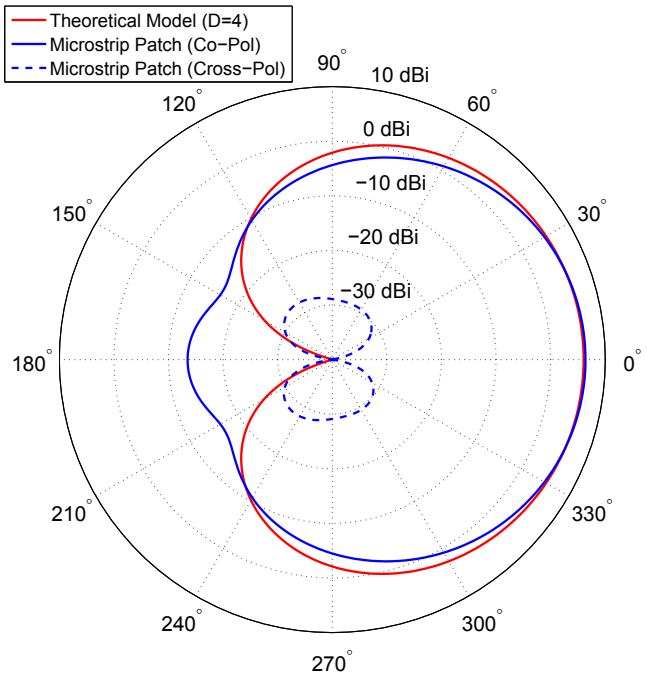

Figure 8: *Directional power patterns from Eqn. (44) with $D = 4$ compared to an EM-simulated isolated microstrip antenna.*

voltages generated at the loads of the array elements for each incident signal ϕ were then stored to generate the array calibration matrix, similar to a field-measurement calibration procedure which could be performed in practice (either in an anechoic chamber or in the field). MATLAB was then used to implement various DOA and beamforming algorithms using the EM-simulated array calibration matrices.

Of course, while a $\lambda/2$ dipole element itself is omnidirectional when in isolation, the presence of the other dipole elements in the array will affect the radiation pattern through mutual coupling, a degree to which depends on the separation of the elements. This mutual coupling can have a significant impact on the array response vector when the antenna element spacing is small relative to the wavelength, λ, and in fact can be used to improve dipole array DOA performance through phase ambiguity resolution as long as this gain variation is included in the ARV. To illustrate the impact of mutual coupling on both the dipole array and microstrip array, EM simulations were performed at various element separations. Shown in Fig. 9 is the gain of a single dipole and a single microstrip antenna in Fig. 7 for UCA radii of $r = \lambda/3$, $r = \lambda$, and $r = 5\lambda$.

In isolation, the gain of a dipole antenna would obviously be equal at all angles, however, as shown in Fig. 9, the gain varies significantly at various azimuth angles

(over 8 dB variation for $r = \lambda/3$) due to mutual coupling, effectively turning the dipoles into weakly directional antennas. This illustrates the importance of including the gain in array calibration matrices even when omnidirectional elements are used, particularly for small element separations. For the $\lambda/2$ dipole elements, as $r \to \infty$, the gain approaches a constant value for all azimuth angles of approximately 2.0 dB (the slight impedance mismatch at the 50 Ω load reduces the effective gain to 2.0 dB from the theoretical perfectly matched gain of 2.15 dB).

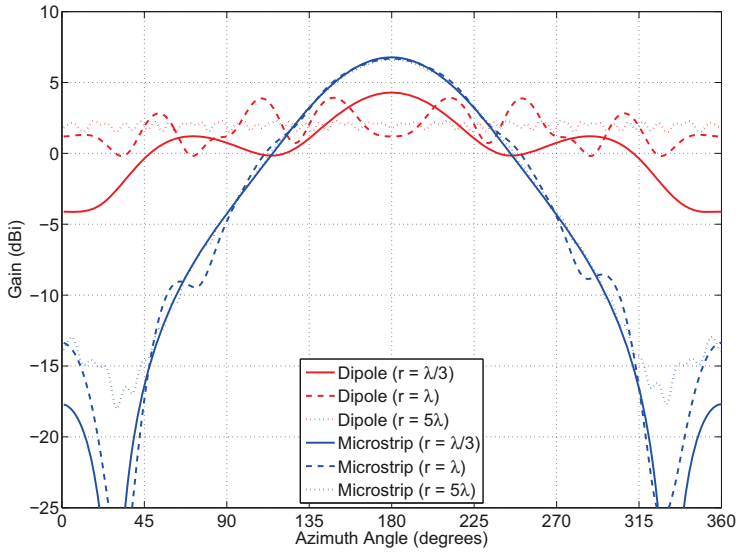

Figure 9: *The effects of mutual coupling on the gain of a single element in 4-element dipole and microstrip arrays for array radii:* $r = \lambda/3$, $r = \lambda$, *and* $r = 5\lambda$.

Shown in Fig. 10(a) is the spatial spectrum of 4-element dipole and microstrip UCAs with $r = \lambda/2$ produced from two incident signals at $\phi = 180°$ and $\phi = 190°$ with SNRs of 20 dB using the MUSIC algorithm. Several conclusions are apparent from this figure. First, in Fig. 10(a), it is clear that ambiguities are present in the dipole array at integer multiples of $\phi = 90°$, which is to be expected for an incident signal at exactly $\phi = 180°$ in a UCA with radius $r = \lambda/2$. The incident signal at $\phi = 190°$ does not show this periodic response because there is no phase ambiguity for the dipole array at this incident angle. Note that in the microstrip array, there are no ambiguities since the gain patterns of the elements are used to distinguish between incident signals arriving at the potential ambiguous angles. Fig. 10(b) shows the spatial spectra of 4-element dipole and microstrip UCAs with $r = 5\lambda$ from a single incident signal at $\phi = 180°$ with a SNR of 20 dB. The large element spacing results in many ambiguous DOA estimates for dipole antennas whereas there is a single clearly defined accurate DOA with microstrip elements.

In a high-SNR environment, the dipole ambiguities for a UCA with $r = \lambda/(2\sqrt{2})$

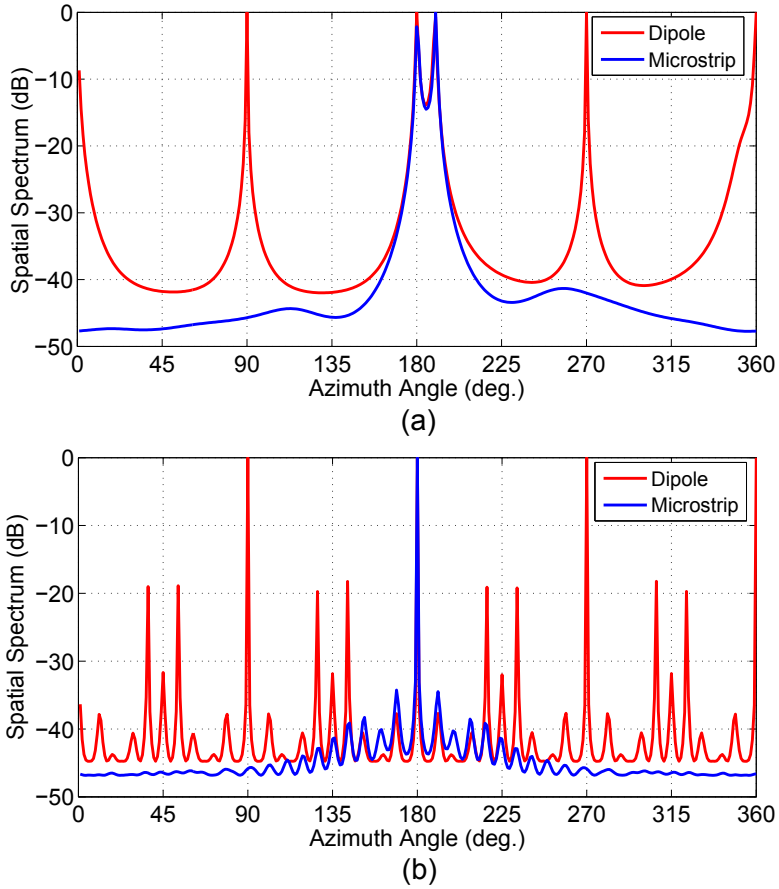

Figure 10: *(a) 4-element, $r = \lambda/2$, dipole and microstrip UCA responses to 20 dB SNR incident signals from $\phi = 180°$ and $\phi = 190°$ using the MUSIC algorithm. (b) 4-element, $r = 5\lambda$, dipole and microstrip UCA responses to a single 20 dB SNR incident signal from $\phi = 180°$ using the MUSIC algorithm.*

would only occur at singular incident angles of exactly $45°, 135°, 225°$, and $315°$. However, in a low-SNR environment, the azimuth angles over which potential ambiguities can occur increases significantly. For example, consider Fig. 11 which sweeps the incident signal ϕ from $1°$ to $360°$ in increments of $1°$ (each angle's RMSE computed from 1000 runs as described previously). In this figure, it is clear that the DOA estimation RMSE increases significantly at incident angles within approximately $\pm 15°$ of the odd-integer multiple $45°$ ambiguity points in the dipole array. In contrast, no such ambiguities occur with the microstrip array, since the gains of the elements are strongly dependent on ϕ and this information is used in addition to the phase information. At points in between the ambiguity angle areas the performance of the dipole array and the microstrip array are similar. Even with UCA radii less than the point at which ambiguities should occur, for example, at $r = \lambda/3$, in low-SNR con-

ditions dipole arrays still can produce erroneous results from ambiguous estimates, which does not occur in a microstrip array.

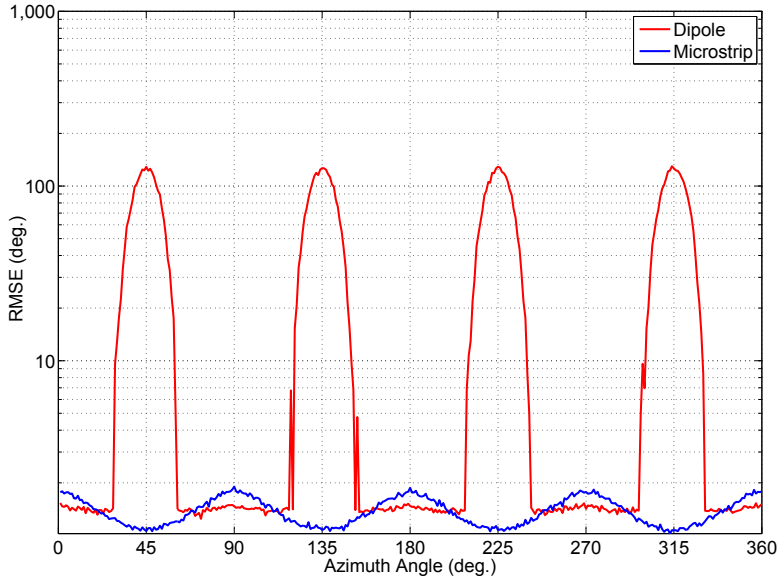

Figure 11: *4-element dipole and microstrip UCA DOA estimation RMSE from a 0 dB SNR swept azimuth angle incident signal from* $\phi = 1°, 2°, \ldots, 360°$ *using the MUSIC algorithm (1000 runs at each angle).*

Shown in Fig. 12 are the DOA estimation errors over all azimuth angles for the 4-element UCAs with dipoles and microstrip elements (1000 runs per angle). Note that it is possible for the RMSE to conceal very high estimation errors at particular angles if the estimates are accurate over the majority of the incident angles. Obviously this is a very undesirable characteristic since it would diminish the confidence in the DOA estimate. It was found that this behavior did not occur for the microstrip patch designed and simulated in this section and that the estimation error was approximately constant across all azimuth errors.

Since the width of the substrate, W_{sub} equals $\lambda/2$, the minimum possible array radius is $r = \lambda/4$ and at this value there is no separation between the substrates. The results show that the RMSE is approximately equal for $r < \lambda/(2\sqrt{2})$, however, at larger radii, the dipole error increases significantly due to the phase ambiguity problem discussed earlier. In contrast, the DOA estimation error remains relatively constant using microstrip elements. It is interesting to note that the reason for the approximately equal performance at small array radii is due in part to the mutual coupling in the dipole array effectively creating directive elements (see Figs. 3 and 9 with the effective directivities being approximately $D = 3$ for the dipole elements.

While Fig. 12 shows a variable array radius, this is equivalent to a broadband oper-

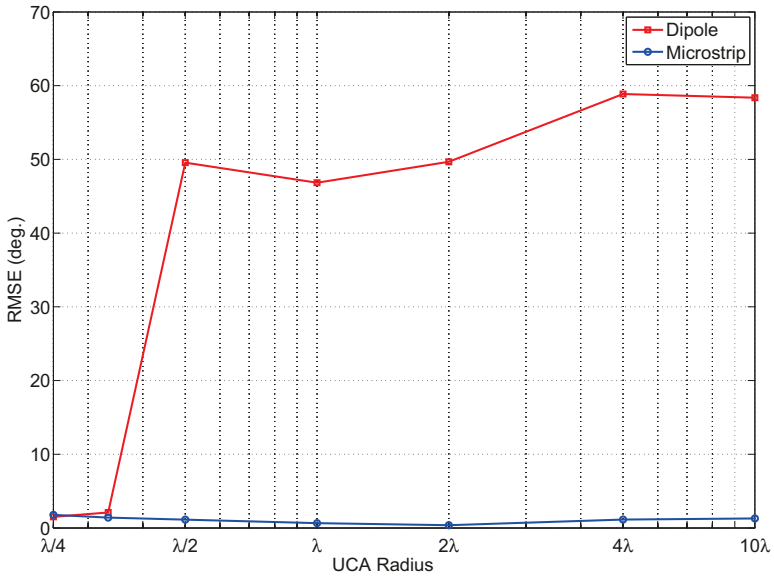

Figure 12: *4-element dipole and microstrip UCA DOA estimation RMSE from a 0 dB SNR incident signal for various array radii using the MUSIC algorithm (logarithmic x-axis).*

ational frequency range assuming the antenna elements have constant characteristics over the band. By using the proposed directive elements for DOA estimation in UCAs, the DOA error becomes much less sensitive to the array radius compared to dipoles and the DOA system bandwidth is limited only by the antenna element itself (i.e., the bandwidth over which the antenna element is matched and maintains a relatively constant radiation pattern). Furthermore, at high carrier frequencies such as millimeter-wave, it may be attractive to use a large array radius and at these high frequencies the directional elements themselves could be designed to be very physically small.

5 Dipole UCA design and fabrication

5.1 Design considerations

The dipole arrays discussed in this report thus far consisted of ideal dipoles in free space. Any implementation of a practical dipole array requires a supporting structure for the dipole elements which will have an effect on the array performance. In general, if a behaviour similar to ideal dipoles in free space is desired, non-conductive material should be used with relative permittivity and permeability close to unity. A design frequency of 1.7 GHz was selected for the array which results in a dipole length of approximately 8.8 cm ($\lambda/2$). The array radius was selected to be $r = \lambda/3$ to be slightly less than the maximum unambiguous radius ($r = \lambda/(2\sqrt{2})$) as discussed previously.

Dipoles require a balanced feed in order to produce an omnidirectional far-field radiation pattern. Typically, antenna arrays are connected using coaxial cables, which support unbalanced (or single-ended) signals. Therefore, a conversion from an unbalanced to a balanced signal is necessary for each dipole element in the array which can be accomplished with the use of a balun. There are a variety of techniques that can be used to implement a balun, and they can be divided into two general categories: active and passive. Active baluns use transistors to perform the conversion from unbalanced to balanced, and passive baluns use components such as transmission lines, inductors, capacitors, transformers, etc. [41]. Active baluns are very attractive in RF/microwave integrated circuits due to their compact physical size, however, in general, passive baluns are much more common in the RF/microwave field.

In order to simplify the fabrication of the proposed dipole UCA, active elements, lumped elements, and transformers were avoided, and a balun known as a microstrip tapered balun was chosen to provide a balanced feed to the elements. This type of balun can have a wide bandwidth, requires only printed transmission lines, and can be integrated into the dipole array supporting structure.

5.2 Microstrip tapered balun

A microstrip tapered balun, shown in Fig. 13, is a transmission line structure that at one side is a microstrip line (unbalanced) and transitions into a parallel strip line (balanced) [42, 43, 44, 45, 46, 47]. A microstrip transmission line is a quasi-transverse electromagnetic mode (TEM) transmission line where the signal trace is on one side of the printed circuit board (PCB) and a ground plane (often assumed to be infinite in extent for ease of analysis) is on the other side. For a given substrate, the width of the signal trace determines the characteristic impedance of the transmission line. Parallel strip lines have traces of equal width on both sides of the PCB (this width determines the characteristic impedance for a particular substrate).

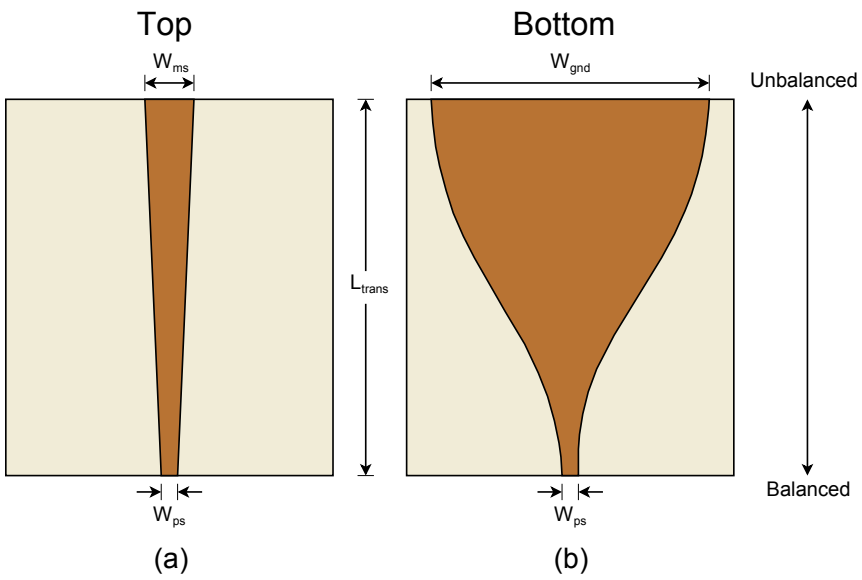

Figure 13: *(a) Top view of the microstrip taper balun. (b) Bottom view of the microstrip taper balun.*

Various types of transitions are possible with microstrip tapered baluns including linear, exponential [47], Hecken [45], and Klopfenstein [46]. Generally, a taper is required on the top conductor as well as the bottom in order to obtain the desired characteristic impedances. The taper of the top conductor is generally much less significant than the taper of the bottom conductor and a simple linear taper is the most common. While a linear taper would be the simplest to design for the bottom conductor as well, this can result in the requirement of a longer taper length and/or a degraded input reflection coefficient compared to other possible transition types. While a Klopfenstein taper can provide the minimum transition length for a particular reflection coefficient requirement, its design is complex [46]. As a compromise, an exponential taper was used for the proposed balun for the bottom conductor. The width of the bottom conductor as a function of distance l from the unbalanced end to the balanced end can be determined from [47]:

$$w_{bot}(l/L_{trans}) = w_{gnd}\ e^{\left[\left(\frac{l}{L_{trans}}\right)^{\gamma} \ln\left(\frac{w_{ps}}{w_{gnd}}\right)\right]}, \tag{46}$$

where w_{bot} is the width of the bottom conductor at a distance l from the microstrip end (i.e., $l = 0$ at the unbalanced end and $l = L_{trans}$ at the balanced end). The other parameters in Eqn. (46) are shown in Fig. 13, with the exception of γ which controls the shape of the exponential taper.

The maximum transition length for the four baluns was restricted for the proposed

dipole array design by the desired UCA radius ($r = \lambda/3$) and by the space requirements for four SMA connectors on the board for cable connections. Furthermore, the traditional taper for the bottom conductor shown in Fig. 13(b) was not possible since it was desirable to provide electrical isolation between the baluns for the four antenna elements (to isolate the currents generated by each antenna). An electromagnetic optimization simulation was performed and it was determined that $\gamma = 2.5$ produced the optimal transition that resulted in the most suitable combination of accurate phase and amplitude balance and low input reflection coefficient.

Photographs of the top and bottom of the fabricated printed circuit board for the dipole array are shown in Fig. 14. Small circular pads were used as shown at the balanced end of the balun in order to solder the dipole arms to the board. The unique shape of the bottom conductor of the baluns is also clear in this figure which was used to provide isolation between baluns while maximizing the taper transition length.

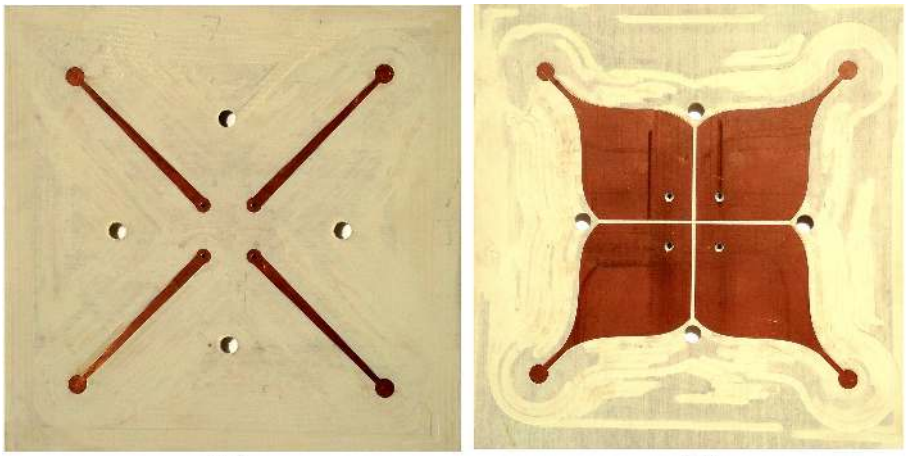

Figure 14: *Photographs of (a) top-side and (b) bottom-side of the dipole array printed circuit board with four integrated tapered microstrip baluns.*

The performance of the balun was determined through simulations in two ways: (1) a back-to-back configuration to determine the S-parameters; and (2) the magnitude and phase balance of the currents on the parallel strip transmission line where the dipoles are connected. A back-to-back configuration of the balun is necessary to determine the S-parameters since they are generally defined using a port from a signal line to ground (as opposed to between two balanced lines). Therefore, the back-to-back balun configuration has been used in the literature to determine the input reflection coefficient and the insertion loss (e.g., [43, 44, 45, 46]). Shown in Fig. 15 is the S_{11} and S_{21} of the balun, which shows that it is matched from approximately 1.0 GHz to 2.7 GHz (using $S_{11} < -10$ dB as the matching criteria) and that the S_{21} is above

−2 dB up to 2.7 GHz. Note that this S_{21} is for two baluns back-to-back, and therefore the insertion loss of the balun is less than 1 dB up to 2.7 GHz.

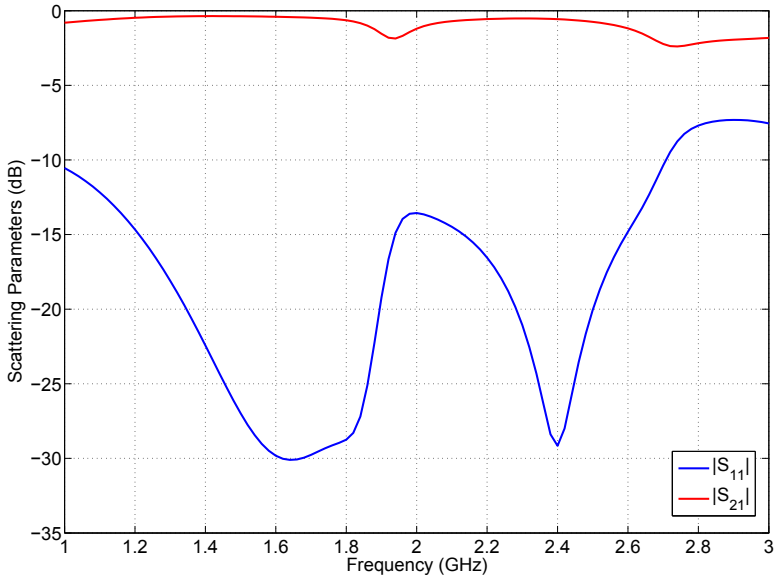

Figure 15: *S-parameters of the back-to-back microstrip tapered balun.*

The simulated amplitude and phase balance for the balun is shown in Figs. 16 and 17 for the frequency range of 1.6 GHz to 2.2 GHz. The amplitude balance was calculated from the magnitudes of the currents on the top and bottom conductors where the dipole arms are connected and would ideally be equal to one. From Fig. 16, the amplitude balance is better than 1.4 from 1.6 GHz to 2.2 GHz. The phase balance, shown in Fig. 17 shows that the phase difference is within 10° of the ideal 180° from 1.6 GHz to 2.2 GHz.

5.3 Complete dipole array

For the proposed dipole array, a ridged low-cost microwave PCB substrate was used, Rogers Corporation RO4835 laminate, with a relative permittivity of 3.66 and a thickness of 1.524 mm (very electrically thin at $< \lambda/100$). Coaxial SMA connectors were soldered to the PCB as described previously and printed microstrip tapered transmission line baluns connected the signals to the dipoles. The arms of the dipole antennas were implemented using copper rods soldered perpendicular to the board. Each arm of the dipole was cut to a length of approximately 4 cm ($\sim \lambda/4$ at 1.7 GHz) to realize an overall length of $\sim \lambda/2$. As shown in Fig. 14, eight holes were drilled in the PCB. The four larger holes were used to secure the array to the mast, and the four smaller holes were used to allow the signal pins of the SMA connectors to pass through the board for soldering on the other side to the signal trace.

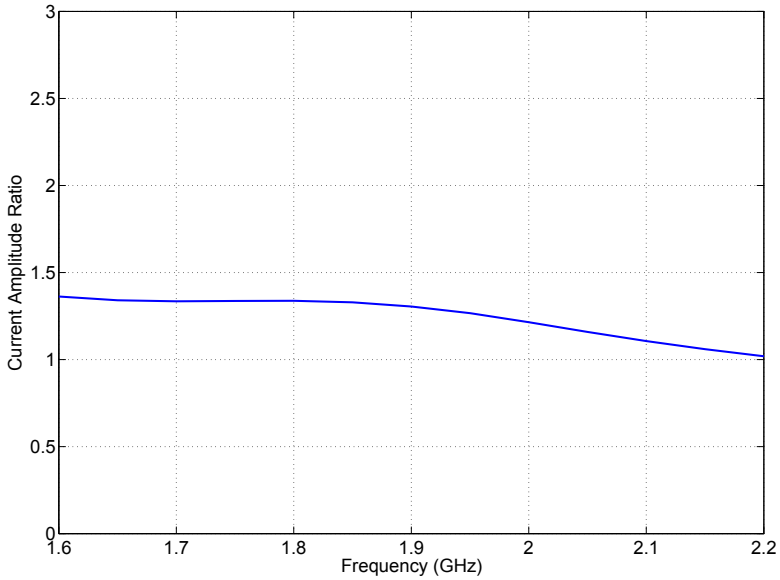

Figure 16: *Microstrip tapered balun amplitude balance.*

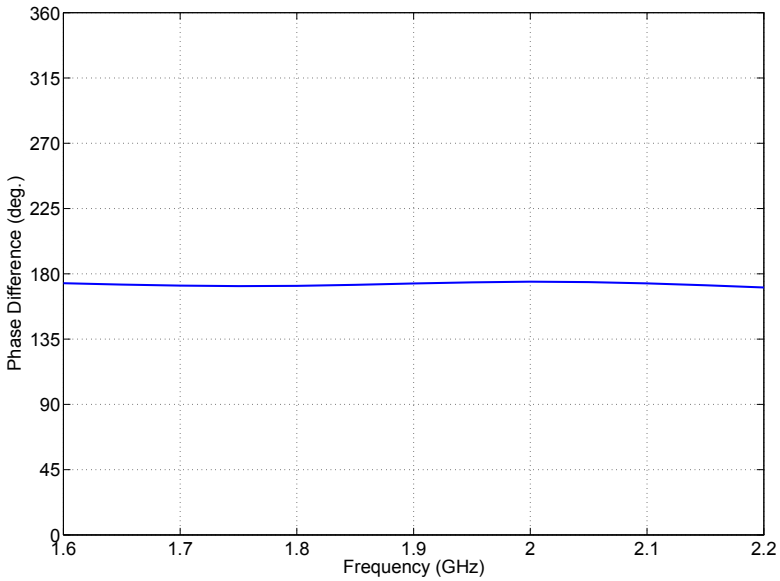

Figure 17: *Microstrip tapered balun phase balance.*

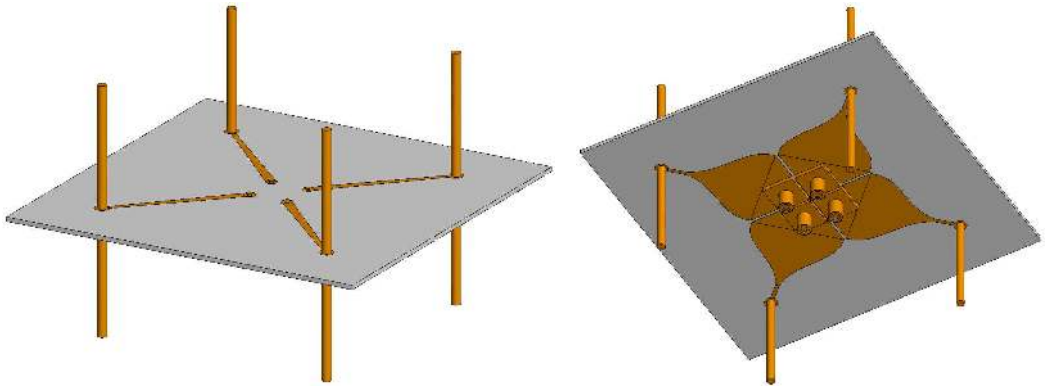

(a) ***(b)***

Figure 18: *(a) Top view of the 3D dipole UCA model with integrated baluns. (b) Bottom view of the 3D dipole UCA model with integrated baluns.*

The 3D model of the dipole array is shown in Fig. 18 and photographs of the completed dipole array are shown in Fig. 19. Fig. 19 also shows the polyvinyl chloride (PVC) piece used to connect the array to the mast and the SMA connectors. Plastic screws were used as opposed to metal in order to minimize the electromagnetic influence.

5.4 Simulation results

An electromagnetic simulation was performed to determine the ARV for the dipole array. The input reflection coefficients were also simulated to determine how well the antennas are matched to the 50 Ω load of the receiver. As shown in Fig. 20, the dipoles are matched ($S_{11} < -10$ dB) from approximately 1.6 GHz to 1.9 GHz. The magnitude and phase ARV responses are shown in Figs. 21 and 22 along with the response of ideal dipoles in free space (dashed lines). Very good agreement between the ideal dipoles and actual dipole array implementation can be seen in this figure, indicating that the microstrip tapered balun is functioning as desired.

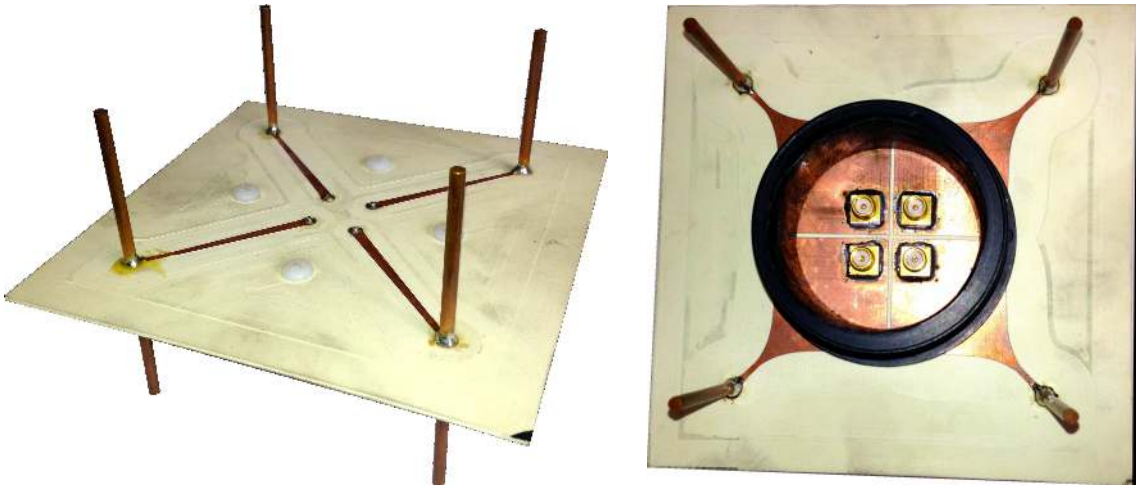

(a) ***(b)***

Figure 19: *(a) Top view of the fabricated dipole UCA with integrated baluns. (b) Bottom view of the fabricated dipole UCA with integrated baluns.*

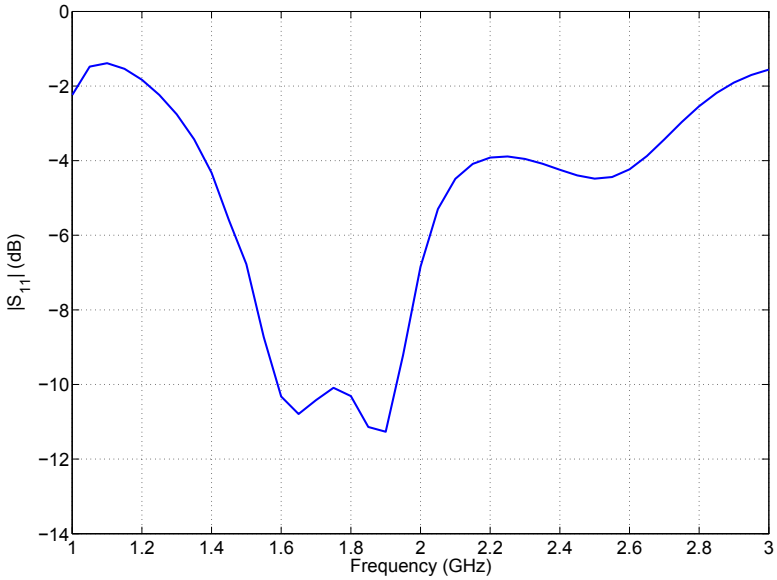

Figure 20: *Simulated input dipole array input reflection coefficients.*

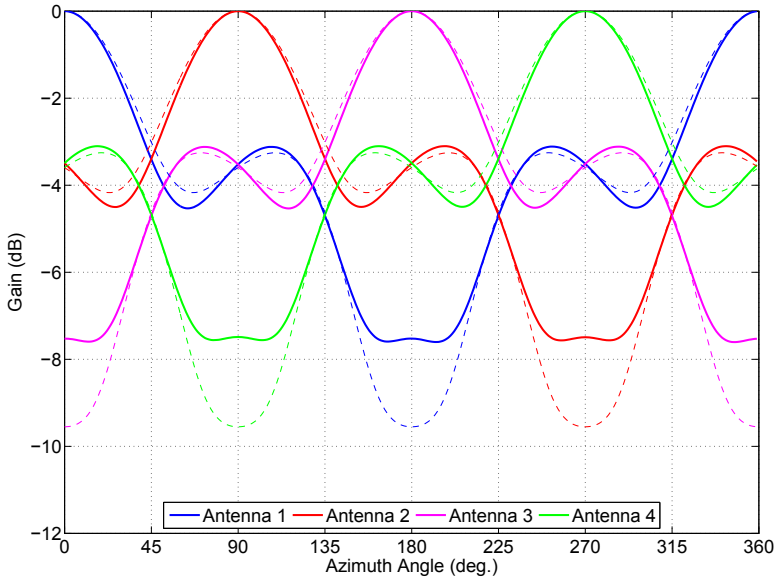

Figure 21: *Dipole array simulated gain patterns (the response of ideal dipoles in free-space are indicated by the dashed lines).*

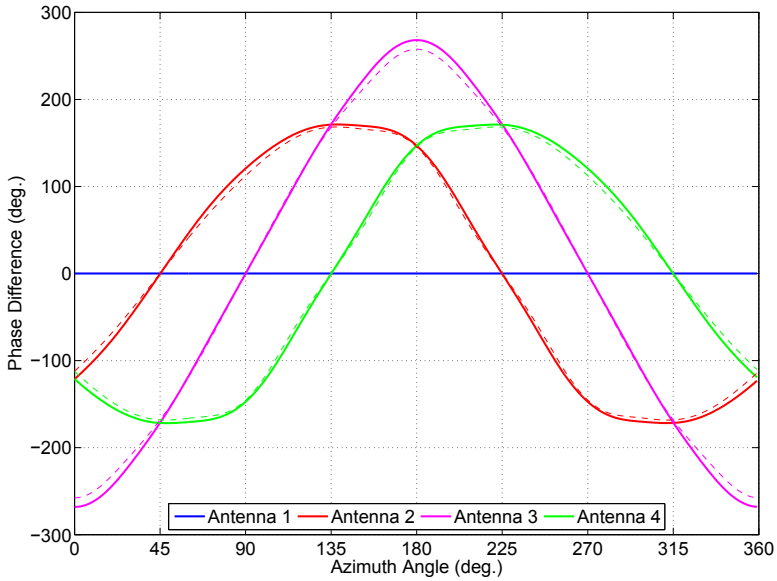

Figure 22: *Dipole array simulated phase differences relative to Antenna 1 (the response of ideal dipoles in free-space are indicated by the dashed lines).*

6 Microstrip UCA design and fabrication

6.1 Microstrip patch elements

The patches described previously in Section 4 were redesigned for a frequency of 1.7 GHz to 1.75 GHz. The performance of the patch antenna was optimized through simulation by using the reflection coefficient and the far-field H-plane radiation pattern as the optimization criteria, as described previously. The dimensions of the substrate were selected to be approximately $2\lambda/3 \times 2\lambda/3$ at 1.7 GHz (11.8 cm $\times$ 11.8 cm) so that an array radius of $r = \lambda/3$ was possible and a direct comparison to the $r = \lambda/3$ dipole array could be made. The substrate for the microstrip patch antennas was a Rogers Corporation RT/duroid 5880 with a relative permittivity of 2.2 and a thickness of 3.175 mm. A photograph of one of the microstrip patch antenna elements is shown in Fig. 23.

Figure 23: *Photograph of a microstrip patch antenna element.*

The narrow-spacing array with $r = \lambda/3$ is shown in Fig. 24 without a mount (the mount for the patches is described in the following section). A wide-spacing version of the array was also developed using the same patches. This array with larger element separation was designed with a radius of $r = 2\lambda$ and is shown in Fig. 25 without a mounting structure.

6.2 Array mounts

The structure that is used to hold the antennas in place can have a significant impact on the array performance. The mounting structures for the two microstrip patch arrays were designed using 3D modelling software and realized on a 3D printer (3D Systems ProJet 260C). The 3D printed material is primarily calcium sulfate dihydrate

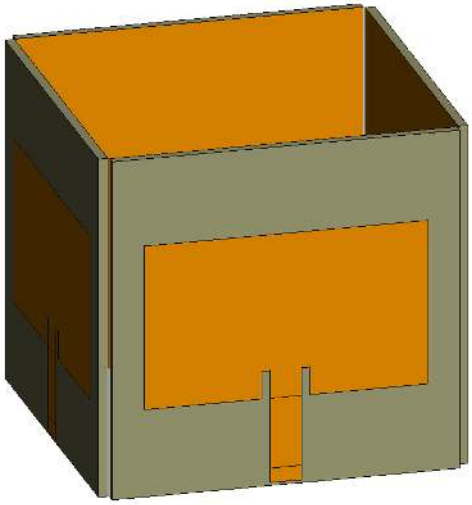

Figure 24: *3D model of the narrow-spacing microstrip patch array used for EM simulations.*

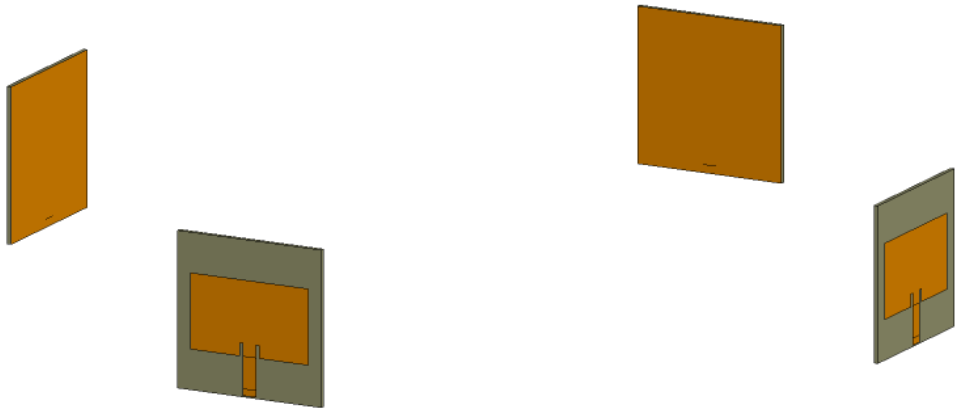

Figure 25: *3D model of the wide-spacing microstrip patch array used for EM simulations.*

along with a resin. The exact electrical properties of the material were not available, and for simulations an electromagnetically transparent material was assumed.

For both arrays, the mounts were designed such that the microstrip patch antennas could easily slide into and out of position and with channels for the cables to follow. Holes were also included for screws that would attach the mount to the mast. Shown in Figs. 26 is a screenshot of the 3D model and a photograph of the fabricated 3D printed mount. Fig. 27 is the final populated narrow-spacing microstrip UCA.

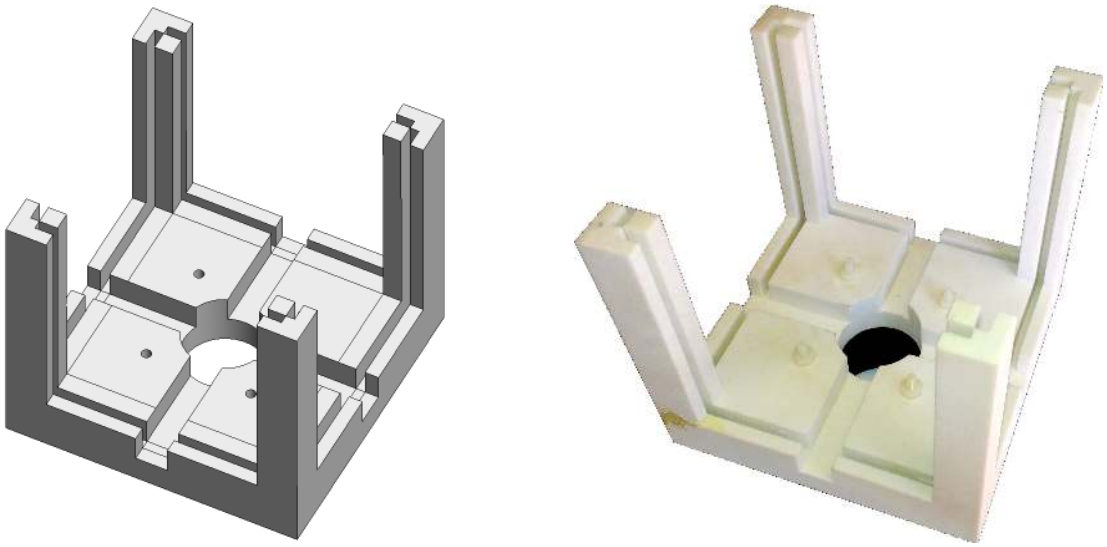

(a) ***(b)***

Figure 26: *(a) 3D model of the narrow-spacing microstrip patch array mount. (b) 3D printed narrow-spacing microstrip patch array mount.*

Four individual 3D mounts were designed for the wide-spacing array, as shown in Fig. 28. These mounts were fastened to plexiglass arms at the appropriate locations to realize a $r = 2\lambda$ UCA radius. A photograph of the completed wide-spacing microstrip patch array is presented in Fig. 29.

6.3 Simulation results

The two microstrip UCAs were simulated in FEKO and their ARVs were produced. The results for the narrow-spacing array are shown in Figs. 30 and 31, and the wide-spacing ARV is shown in Figs. 32 and 33. The normalized magnitude response is similar for the two arrays which is to be expected since the effects of mutual coupling are reduced for a directive antenna array. Also, note the much larger changes in phase difference for the wide-spacing array.

Figure 27: *Photograph of the narrow-spacing microstrip patch array in 3D printed mount.*

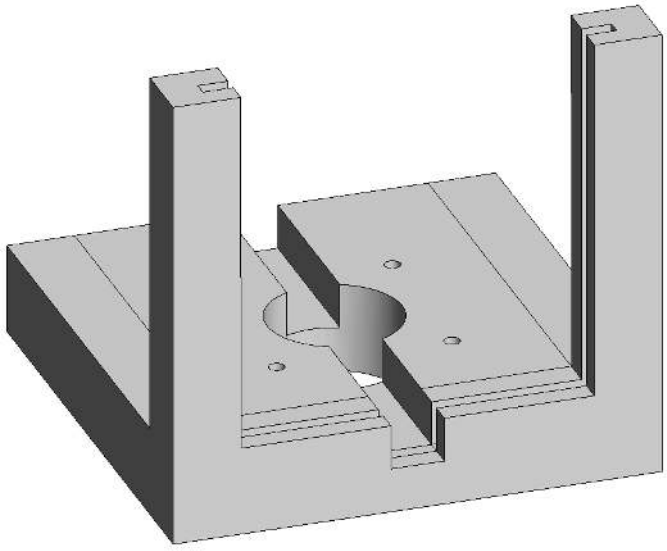

Figure 28: *3D model of the wide-spacing microstrip patch array mount.*

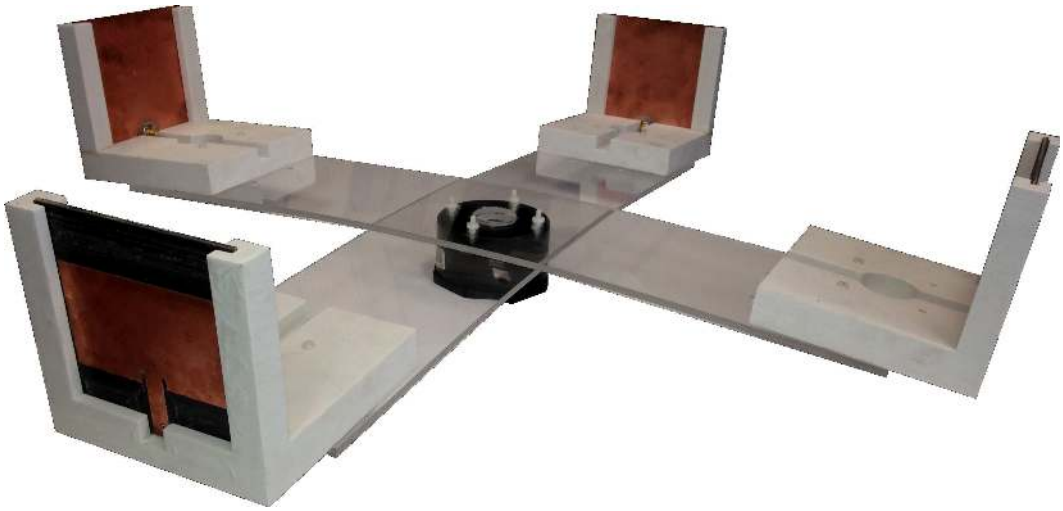

Figure 29: *Photograph of the wide-spacing microstrip patch array.*

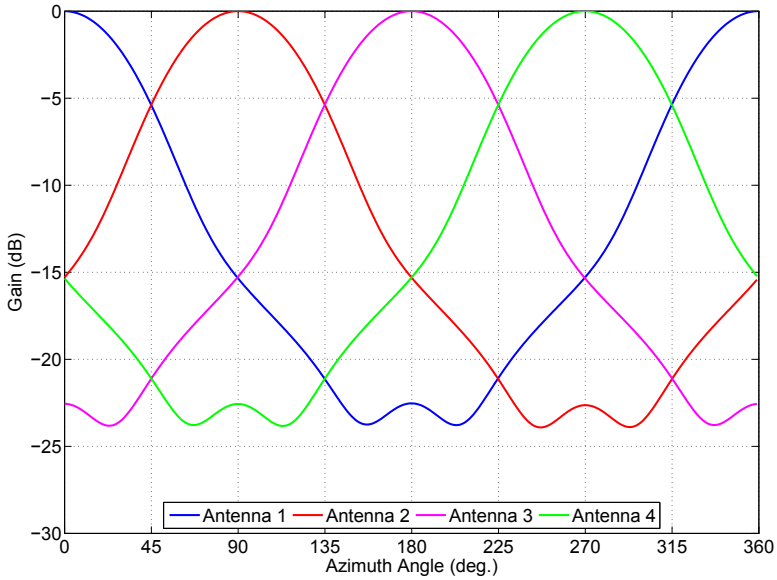

Figure 30: *Narrow-spacing microstrip array simulated antenna gain patterns (normalized).*

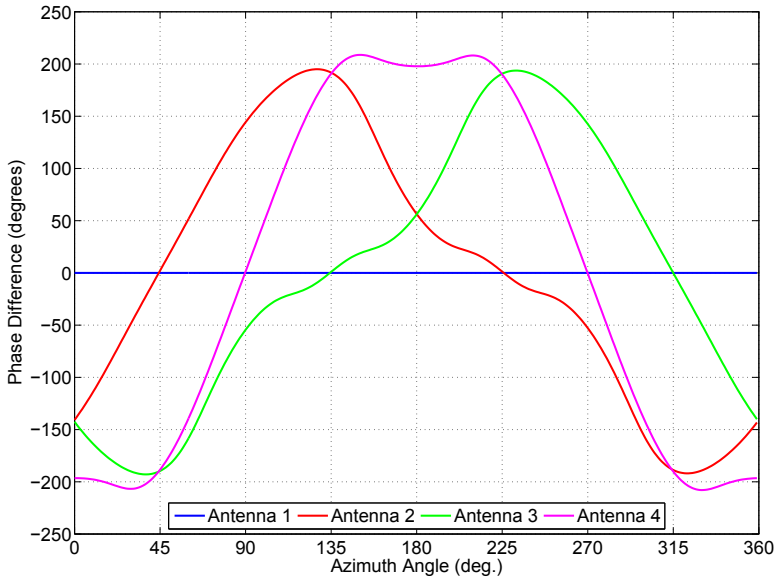

Figure 31: *Narrow-spacing microstrip array simulated antenna phase differences.*

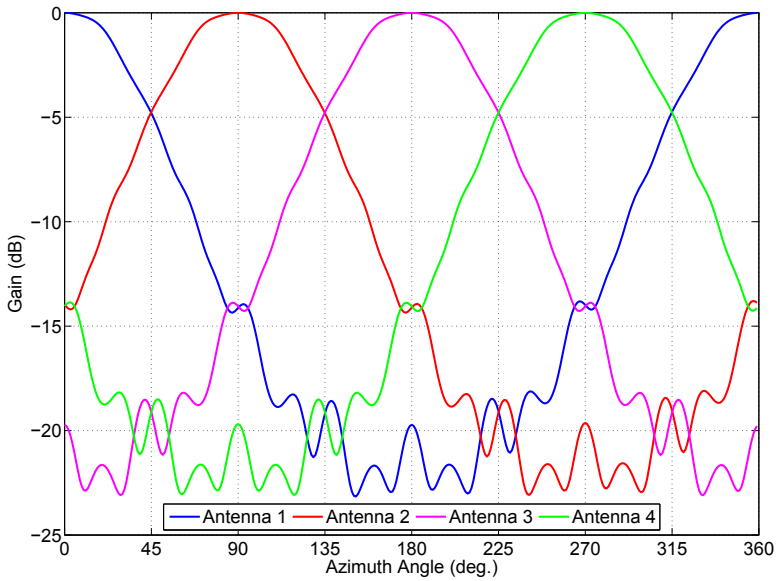

Figure 32: *Wide-spacing microstrip array simulated antenna gain patterns (normalized).*

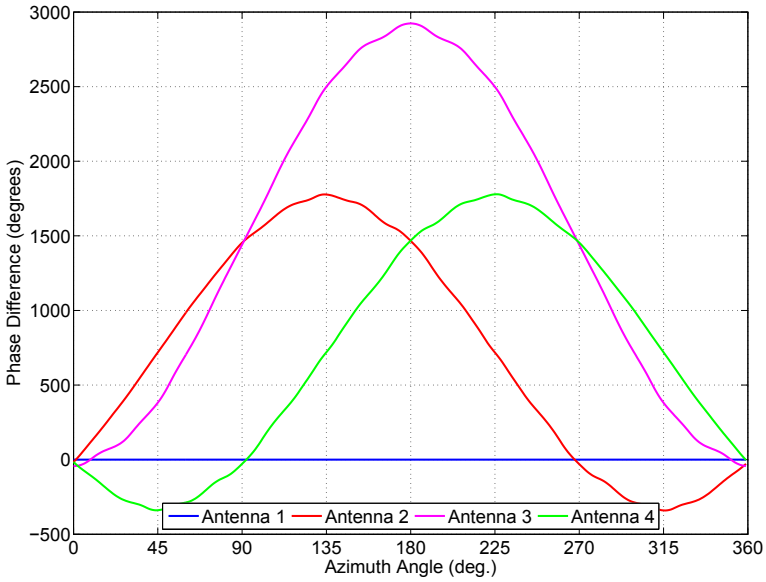

Figure 33: *Wide-spacing microstrip array simulated antenna phase differences.*

7 Anechoic chamber measurement results

7.1 Measurement setup

To measure the performance of the arrays, a radio frequency anechoic chamber was used and the results were compared to the simulations shown previously. The anechoic chamber was approximately 5 m × 10 m and all surfaces were covered with radiation absorbent material (RAM). The antenna measurement configuration was for far-field radiation patterns, i.e., the region far enough away from the antenna that the radiation pattern no longer changes with distance. The far-field, or Fraunhofer, region requires all three criteria be met:

$$R > 2D^2/\lambda\,, \tag{47}$$

$$R \gg D\,, \tag{48}$$

$$R \gg \lambda\,, \tag{49}$$

where R is the distance from the antenna, and D is the largest linear dimension of the antenna. For the antennas in this work (including the transmitting antenna used for measurement), the maximum linear dimension is approximately 50 cm, thus to measure frequencies down to 1 GHz ($\lambda_{max} = 30$ cm) the separation of the transmitting and receiving antennas must be at least $R = \max(167\text{ cm}, 500\text{ cm}, 300\text{ cm}) = 500$ cm for the far-field criteria, assuming 'much greater than' corresponds to at least an order of magnitude (10×). Therefore, the transmitter and receiving antennas should be separated by at least 5 m which is possible given the dimensions of the anechoic chamber.

Another concern for the measurement of the arrays in the anechoic chamber was the performance of the RAM at the frequencies of interest. The exact specifications for the RAM in the anechoic chamber was not available, so the performance of RAM with comparable dimensions was used to give an indication of their characteristics. 18 inch pyramidal absorbers similar to the ones installed in the chamber generally have a maximum of −40 dB reflection at 1 GHz for normal incidence which is acceptably low for the measurements required to characterize the arrays.

The arrays were mounted on top of a 1.5 m PVC pipe with the cables routed through the middle of the pipe. The positioner used to control the azimuth angle of the array was the Pan-Tilt Unit-D300 RF Antenna Positioner from FLIR Motion Control Systems. The transmitting antenna, shown in Fig. 34, was a standard gain pyramidal horn antenna (ETS-Lindgren model 3160-03). The measurements were recorded with a calibrated Advantest R3860A Vector Network Analyzer (VNA).

The entire measurement system was controlled using custom MATLAB code that was developed by DRDC staff. This software configures the VNA, moves the antenna array to the desired azimuth angle, and records the measurement. A full ARV was

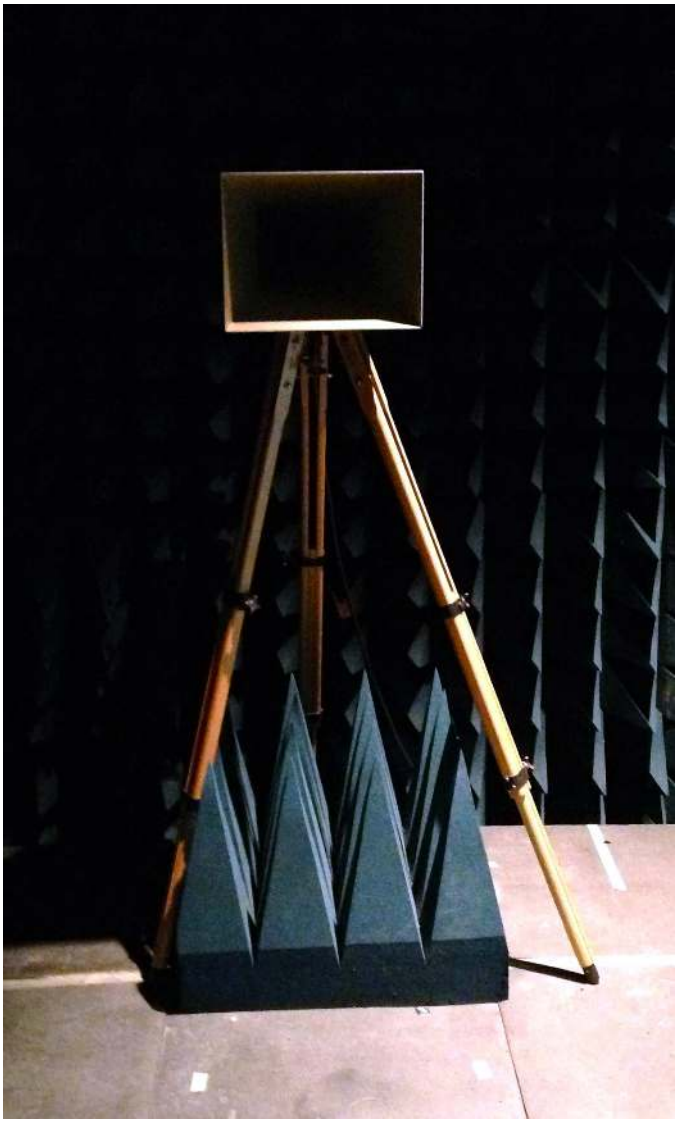

Figure 34: *Standard gain horn antenna (ETS-Lindgren model 3160-03) used as the transmitter in the anechoic chamber. The flat surface upon which the antennas are mounted are walkway absorbers (i.e., RAM with a flat support structure on top).*

automatically measured by recording measurements at 1° increments over the full 360° of azimuth angles.

7.2 Dipole UCA results

The dipole array was set up in the anechoic chamber, connected to the VNA, and oriented properly in relation to the transmitting horn antenna. The input reflection coefficient (S_{11}) was measured for each of the four antennas from 1 GHz to 3 GHz and the results are shown in Fig. 35. Using −10 dB as the threshold, the antennas are matched between 1.6 GHz and 1.9 GHz. The ARV for the dipole array was measured by recording the magnitude and phase response for the antennas for every 1° increment of ϕ. The measured ARV normalized magnitude response is presented in Fig. 36.

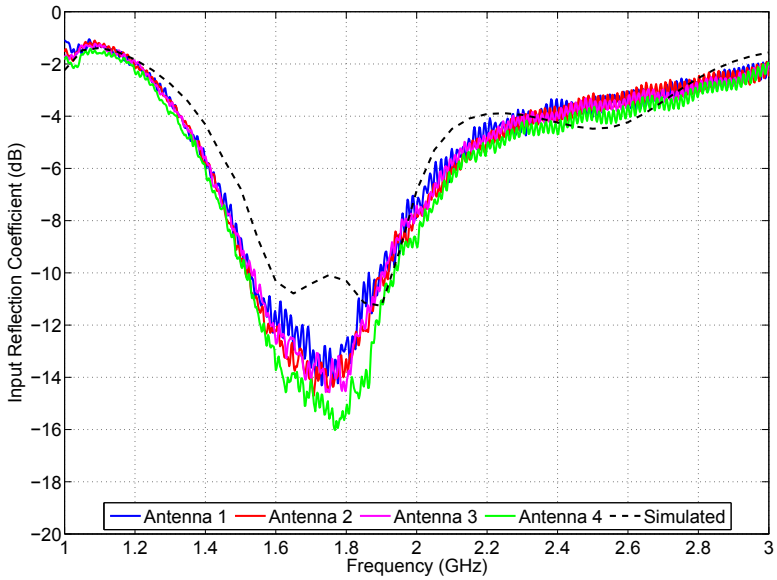

Figure 35: *Measured input reflection coefficients of the dipole UCA antenna elements (simulation results shown with a dashed line).*

Figs. 35 and 36 show that the simulated results are generally accurate but there are some differences. The antenna cables, which run directly down from the centre of the array are significant conducting surfaces (four coaxial cable ground shields), which were not included in the simulations and are a likely cause of the deviations between the measured and simulated results.

The dipole array phase response is shown in Fig. 37 with the phase of Antenna 1 used as the reference. Close agreement between the simulation and measurement results can be seen in this figure with the exception of Antenna 3 which is offset from the

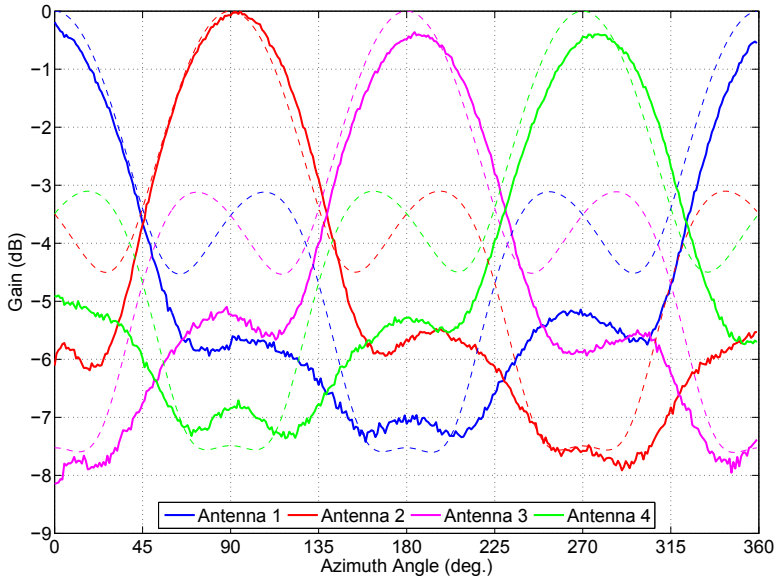

Figure 36: *Dipole array measured normalized gains at* 1.7 *GHz (simulated results shown with dashed lines).*

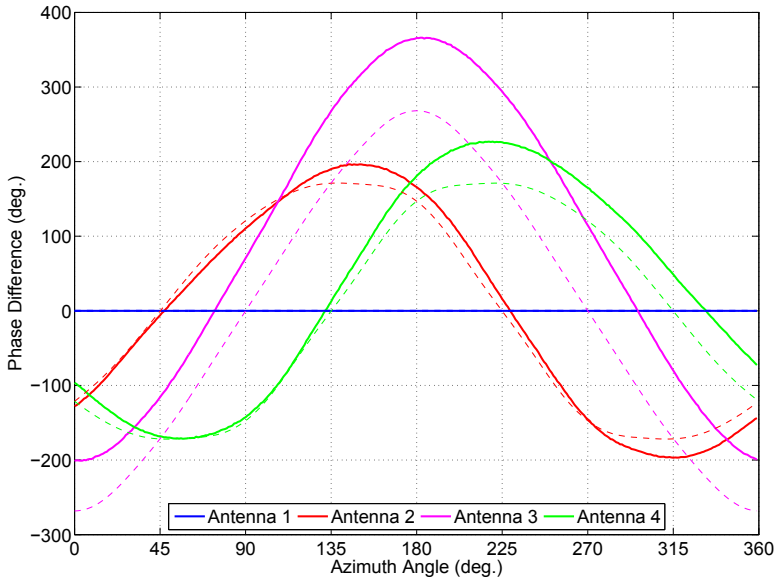

Figure 37: *Dipole array measured phase differences at* 1.7 *GHz relative to Antenna 1 (simulated results shown with dashed lines).*

simulation results. Since it was desired to potentially test the arrays in the field, the cables were not calibrated out of the measurement with the VNA. This was so that when the cables are connected to a 4-channel receiver in the field the ARV generated in the chamber would still be valid. While the same cable model was used for all four antennas, they would not be precisely the same length, and the adaptors used would show similar variations. At 1.7 GHz, a phase shift of 90° corresponds to a change in length of approximately 4 cm, which could explain the phase offset shown for Antenna 3 in Fig. 37.

7.3 Microstrip patch UCA results (narrow-spacing)

The narrow-spacing microstrip patch array was installed in the chamber for measurement using the same measurement configuration as the dipole array. The input reflection coefficients for the four antenna ports is shown in Fig. 38. From this figure, the bandwidth of the array is from 1.7 GHz to 1.74 GHz using −10 dB as the threshold.

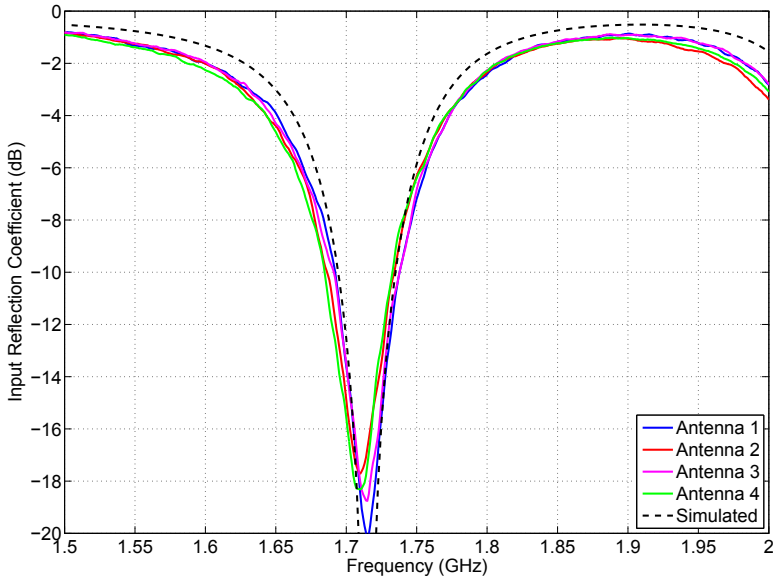

Figure 38: *Measured input reflection coefficients of the narrow-spacing UCA antenna elements (simulation results of a single microstrip patch in isolation is shown with a dashed line).*

The ARV for this array was measured for 1° increments in azimuth angle and the results are shown in Figs. 39 and 40. The measured normalized magnitude response follows the simulation results closely with the exception of when the antenna is facing away from the transmitter. It is possible that the increased magnitude in the measured results at these angles could be due to the proximity to the back wall of

the anechoic chamber (the patch is pointing at the back wall over these angles). The general trends in the simulated phase results are confirmed in Fig. 40, and similar to the dipole array there is a phase offset for Antenna 3 which is consistent with the explanation given previously of a different cable/connector length for this antenna. Other variations between the simulated and measured results can be explained by the presence of cables and the mount, which were not included in simulations.

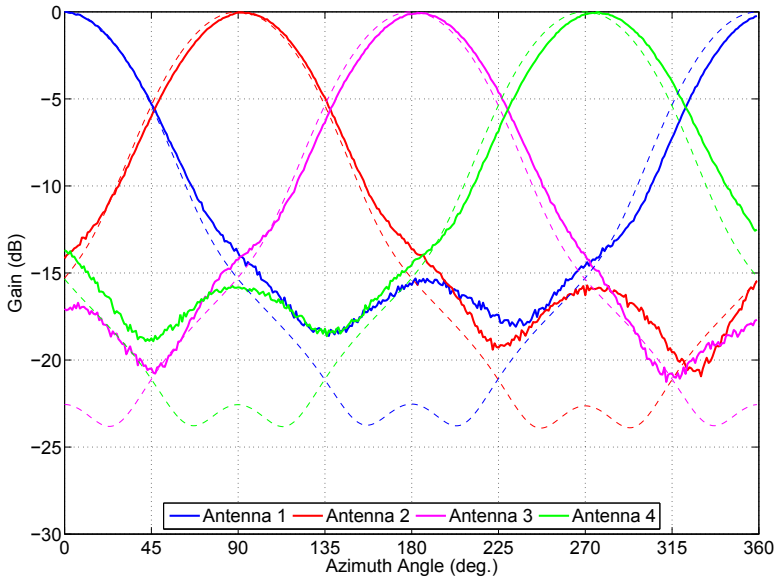

Figure 39: *Measured narrow-spacing microstrip array antenna normalized gain patterns at* 1.7 *GHz (simulation results shown with dashed lines).*

7.4 Microstrip patch UCA results (wide-spacing)

A similar test procedure was conducted for the wide-spacing microstrip patch antenna array. The input reflection coefficient for each antenna is shown in Fig. 41, which is very similar to the narrow-spacing result which was expected since the directional characteristics of the microstrip patch antenna reduce the effects of mutual coupling relative to omnidirectional elements.

The magnitude and phase of the ARV is shown in Figs. 42 and 43. The measured results closely follow the general characteristics of the simulated results and will be used to estimate the DOA in the following section.

7.5 DOA estimation/ARV verification

In order to verify the measured ARVs as well as test the DOA estimation algorithms, a DOA testbed was developed by DRDC staff and the arrays were tested in an anechoic

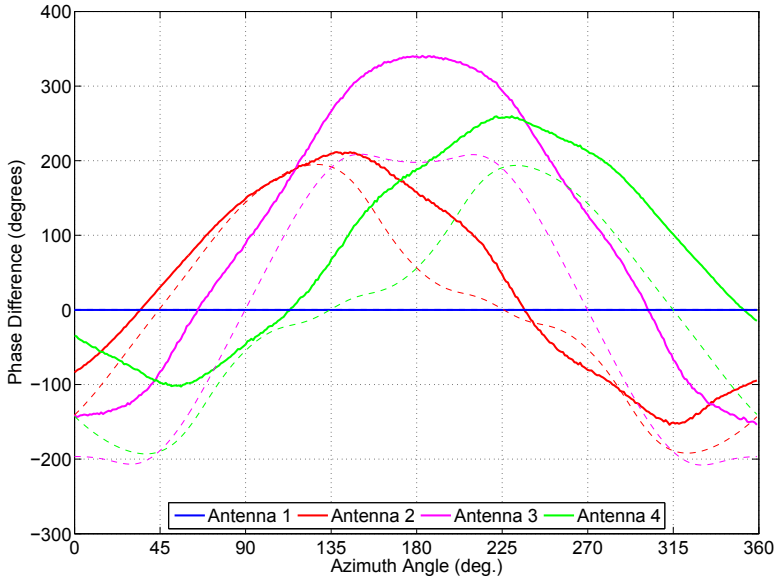

Figure 40: *Measured narrow-spacing microstrip array phase differences relative to Antenna 1 at* 1.7 *GHz (simulation results shown with dashed lines).*

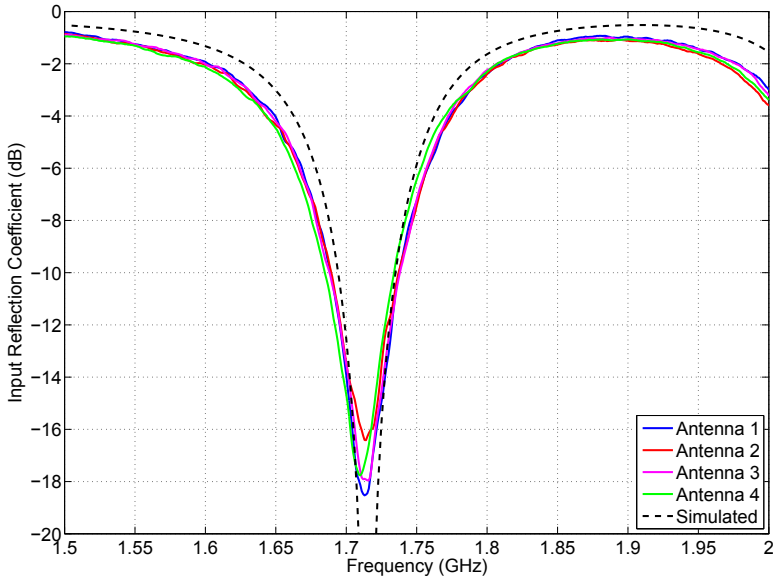

Figure 41: *Measured input reflection coefficients of the wide-spacing UCA antenna elements (simulation results of a single microstrip patch in isolation is shown with a dashed line).*

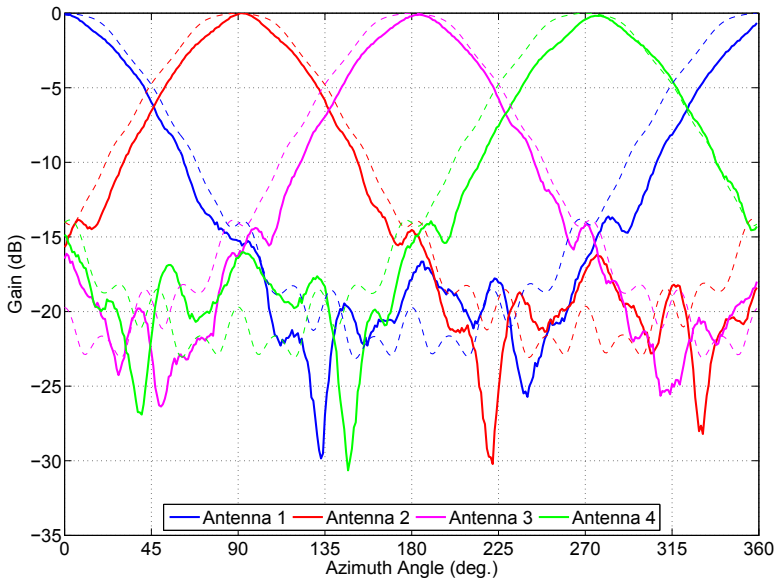

Figure 42: *Measured wide-spacing microstrip array antenna normalized gain patterns (simulation results shown with dashed lines).*

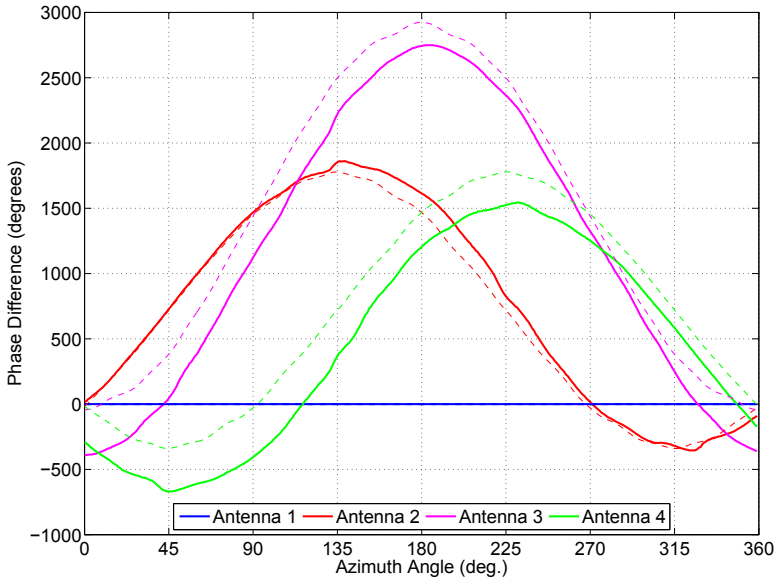

Figure 43: *Measured wide-spacing microstrip array phase differences relative to Antenna 1 (simulation results shown with dashed lines).*

chamber. For a particular azimuth angle, data was recorded for the four antenna channels and processed to produce a DOA estimate. The synchronized and calibrated four channel receiver was implemented using two dual-channel DRS Nanoceptors (SI-9144) for the RF front-ends and four National Instruments Universal Software Radio Peripherals (USRPs) N210s for signal digitization and IQ data transfer to a PC.

An example of the measured MUSIC and CBF spatial spectra for the dipole array with a 1.7 GHz incoming signal at 180° is shown in Fig. 44. From this figure, it is clear that either algorithm could be used to accurately estimate the signal's incident angle, however, as expected, MUSIC produces a much higher resolution response. Similarly, the CBF and MUSIC responses for the two microstrip arrays are shown in Figs. 45 and 46. Note that the wide-spacing microstrip UCA produces a more narrow peak in the MUSIC spatial response, but that the CBF is not as accurate in the wide-spacing array.

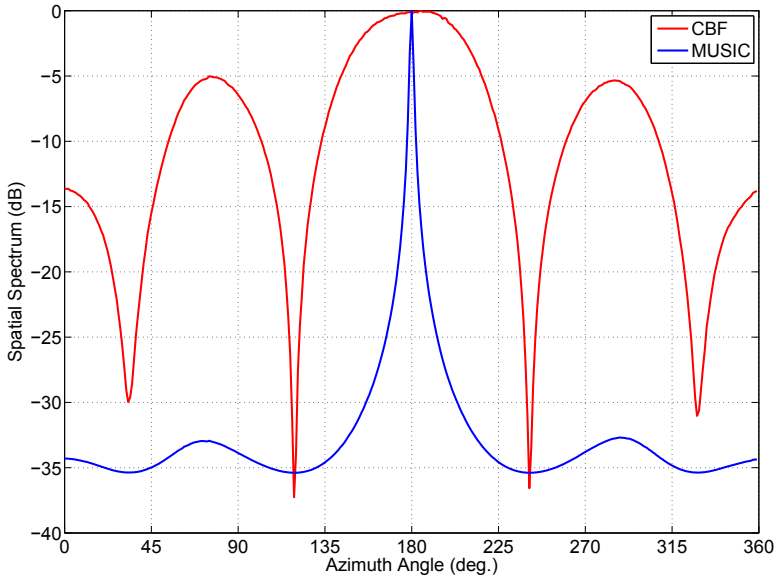

Figure 44: *Measured dipole array spatial spectrum for a* 1.7 *GHz incoming signal at* 180° *for the classic beamformer and MUSIC algorithms.*

In order to determine the overall performance across azimuth for the arrays, at each 1° increment of ϕ over the full 360°, five runs were performed with a DOA computed for each. This resulted in a total of 1800 DOA estimates per array. The RMSE for the three arrays is shown in Fig. 47 with the RMSE computed at each 1° increment from the five runs. The worst-case error for all arrays and angles was 2°, and the overall RMSEs from each array's 1800 runs were as follows: Dipole Array: 0.01°, Microstrip Array (narrow-spacing): 0.4°, and Microstrip (wide-spacing): 0°. It was found that the wide-spacing microstrip array produced perfect results over the 1800

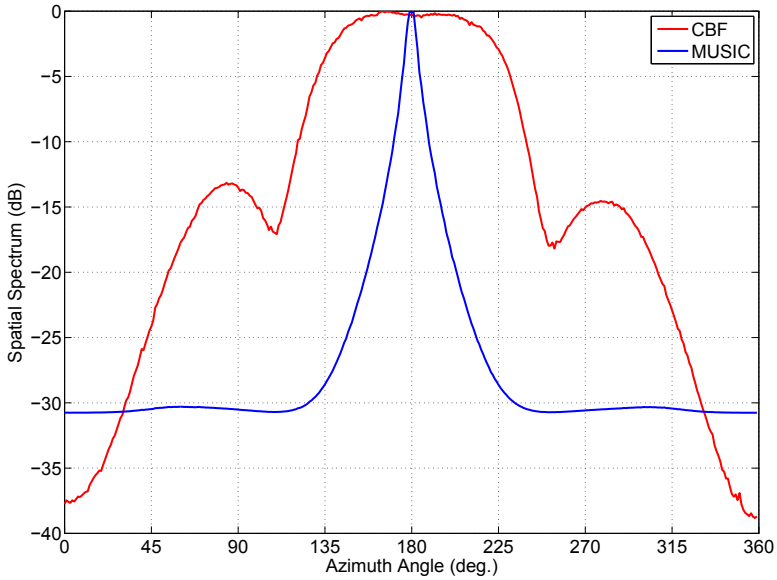

Figure 45: *Measured narrow-spacing microstrip patch array spatial spectrum for a* 1.7 *GHz incoming signal at* 180° *for the classic beamformer and MUSIC algorithms.*

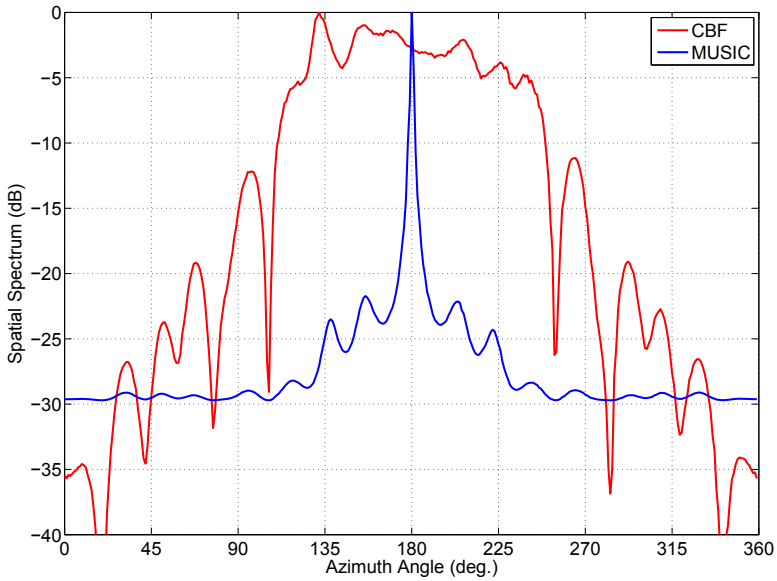

Figure 46: *Measured wide-spacing microstrip patch array spatial spectrum for a* 1.7 *GHz incoming signal at* 180° *for the classic beamformer and MUSIC algorithms.*

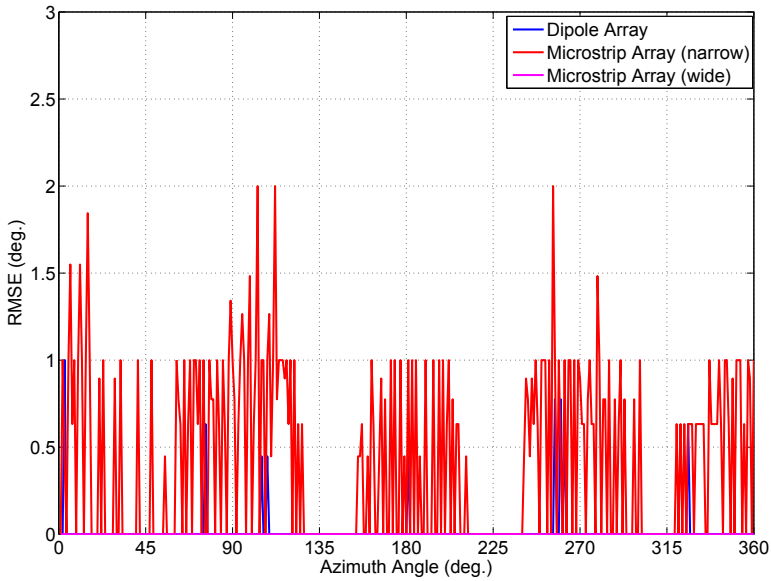

Figure 47: *Measured RMSE for all three arrays (five runs per* 1° *increment in azimuth angle).*

runs. Clearly all three arrays produce accurate DOAs, which is to be expected since the DOA tests were conducted in the same environment as the ARVs were measured.

8 Recommendations and future work

The theory, simulations, and measured results presented in this report show the potential for new antenna arrays that can achieve improved direction finding performance. In particular, the benefits of using directional antenna elements in UCAs was discussed in detail and it appears that further improvement through antenna element optimization is possible. It may be possible through future work to mathematically determine the radiation pattern that minimizes the CRLB for a particular number of elements and array radius. An antenna element that approximates this pattern could then be designed and tested. Of course, it is possible that the mathematically-optimal radiation pattern may not be realizable in a practical antenna. Given the practical possibilities for far-field gain patterns of potential antenna elements, the set of radiation patterns may be restricted and could result in further simplifications to the CRLB. Standard optimization procedures could be used to determine the overall optimum array design that minimizes DOA estimation error by finding the parameters that minimize the CRLB.

The value of antenna element directivity that minimizes the CRLB increases with more UCA elements and decreases with a larger array radius. For a UCA with $N = 4$ elements, a directivity in the range of $D = 2$ to $D = 10$ produces a low CRLB for a wide range of array radii (from $r = \lambda/10$ to 10λ) using elements with radiation patterns similar to a microstrip patch (primarily unidirectional). For a UCA with $N = 8$ elements this ideal directivity increases to roughly $D = 10$ to $D = 30$.

Through simulations and measurements it was found that a wide-spacing microstrip patch UCA produces the most accurate DOA estimates. However, this array may be more sensitive to errors in the calibrated ARV than more narrowly spaced arrays (particularly phase errors). Therefore, field testing of a UCA with a large array radius is recommended.

While this report focused solely on UCAs, similar work could be undertaken for other array geometries such as ULAs and V-shaped arrays. In addition, the platforms/vehicles that the antennas are to be mounted on could be taken into consideration since they will have an effect on the antenna element radiation pattern and hence the DOA estimation accuracy. It would also be interesting to investigate the possibility of using the DOA estimates to perform other operations such as jamming or improving communications range through beamforming. This work considered a 2D scenario where both the receiver and the emitter are on the same plane (i.e., both located on the ground). However, the results could be extended to 3D for applications involving airborne platforms or distinct elevation changes.

The results in this report do not include results from practical field measurements. It is expected that the ARVs from simulation and measurements in the anechoic chamber

will not produce accurate results in the field due to the effects of the vehicle platform as well as other environmental effects such as ground-bounce multipath. Therefore, these arrays should undergo field calibration and testing to determine their potential performance in a real-world environment.

Overall, it is recommended that designers of antenna arrays for DF consider the use of non-traditional antenna elements (i.e., antennas other than simple monopoles or dipoles) in order to improve DOA estimation accuracy and reliability, as well as potentially minimize costs through a reduction in the required number of receiver channels.

9 Conclusion

This report has studied antenna element directivity in UCAs to improve direction of arrival estimation accuracy and robustness. The DOA estimation accuracy of ideal isotropic elements was compared to theoretical directional power patterns and it was found through the derived CRLB and simulations that significantly improved accuracy can be obtained with an appropriate directivity. To evaluate this on a realizable antenna, microstrip patches were used in a 4-element UCA and this array achieved similar or improved DOA accuracy relative to a 4-element $\lambda/2$ dipole UCA under a variety of different conditions. Furthermore, it was shown that by using directive elements improved flexibility with respect to array size can be achieved, potentially resulting in a DOA system where the bandwidth is limited only by the broadband performance of the individual antenna elements and not limited by the electrical size of the array.

To verify the theory and simulation results, three antenna arrays were designed, simulated, fabricated, and tested: a dipole array with integrated baluns and two microstrip arrays with different array radii. The arrays were measured in an anechoic chamber and the results were similar to those found through simulations. All three arrays were found to have better than 0.4° DOA estimation RMSE performance in the anechoic chamber over 1800 runs for each array across all azimuth angles with a worst-case error of 2°. With verification in a controlled lab environment complete, field-testing can be conducted to evaluate the performance of these arrays in a practical EM environment.

References

[1] B. R. Jackson, S. Rajan, B. Liao, and S. Wang, "Direction of arrival estimation using directive antennas in uniform circular arrays," *accepted in IEEE Transactions on Antennas and Propagation (in press)*, October 2014.

[2] G. Byun, H. Choo, and H. Ling, "Optimum placement of DF antenna elements for accurate DOA estimation in a harsh platform environment," *IEEE Transactions on Antennas and Propagation*, vol. 61, no. 9, pp. 4783–4791, September 2013.

[3] Z. Ye and C. Liu, "2-D DOA estimation in the presence of mutual coupling," *IEEE Transactions on Antennas and Propagation*, vol. 56, no. 10, pp. 3150–3158, October 2008.

[4] E. Ben-Ari and J. Remez, "Performance verification of a multimodal interferometric DOA-estimation antenna," *IEEE Antennas and Wireless Propagation Letters*, vol. 10, pp. 1076–1080, 2011.

[5] S. Hwang, S. Burintramart, T. Sarkar, and S. Best, "Direction of arrival (DOA) estimation using electrically small tuned dipole antennas," *IEEE Transactions on Antennas and Propagation*, vol. 54, no. 11, pp. 3292–3301, November 2006.

[6] Z. Ye and X. Xu, "DOA estimation by exploiting the symmetric configuration of uniform linear array," *IEEE Transactions on Antennas and Propagation*, vol. 55, no. 12, pp. 3716–3720, December 2007.

[7] Q. Yuan, Q. Chen, and K. Sawaya, "Accurate DOA estimation using array antenna with arbitrary geometry," *IEEE Transactions on Antennas and Propagation*, vol. 53, no. 4, pp. 1352–1357, April 2005.

[8] J. Liu, l. Li, and W. Huazhi, "Investigation of different types of array structures for smart antennas," in *Int. Conf. on Microwave and Millimeter Wave Technology (ICMMT)*, 2008, pp. 1160–1163.

[9] M. R. Islam and I. A. H. Adam, "Perfomance study of direction of arrival (DOA) estimation algorithms for linear array antenna," *Int. Conf. on Signal Processing Systems*, pp. 268–271, 2009.

[10] B. Wu, "Realization and simulation of DOA estimation using MUSIC algorithm with uniform circular arrays," *The 4th Asia-Pacific Conf. on Environmental Electromagnetics*, pp. 908–912, 2006.

[11] L. Rui, S. Xiaowei, C. Lei, L. Ping, and X. Le, "The non-circular MUSIC method for uniform rectangular arrays," *Int. Conf. on Microwave and Millimeter Wave Technology (ICMMT)*, pp. 1390–1393, 2010.

[12] I. D. Longstaff, P. E. K. Chow, and D. E. N. Davies, "Directional properties of circular arrays," *Proc. of the Institution of Electrical Engineers*, vol. 114, no. 6, pp. 713–718, June 1967.

[13] T. Rahim and D. E. N. Davies, "Effect of directional elements on the directional response of circular antenna arrays," *IEE Proc. on Microwaves, Optics and Antennas*, vol. 129, no. 1, pp. 18–22, February 1982.

[14] T. Rahim, "Analysis of the element pattern shape for circular arrays," *Electronics Letters*, vol. 19, no. 20, pp. 838–840, September 1983.

[15] I. D. Longstaff and D. E. N. Davies, "A wideband circular array for H.F. communications," *Radio and Electronic Engineer*, vol. 35, no. 6, pp. 321–328, June 1968.

[16] J. C. Lim and D. E. N. Davies, "Synthesis of a single null response in an otherwise omnidirectional pattern using a circular array," *Proc. of the Institution of Electrical Engineers*, vol. 122, no. 4, pp. 349–352, April 1975.

[17] D. E. N. Davies and M. S. A. S. Rizk, "A broadband experimental null-steering antenna system for mobile communications," *Radio and Electronic Engineer*, vol. 48, no. 10, pp. 509–517, October 1978.

[18] J. R. F. Guy and D. E. N. Davies, "UHF circular arrays incorporating open-loop null steering for communications," *IEE Proc. on Communications, Radar and Signal Processing*, vol. 130, no. 1, pp. 67–77, February 1983.

[19] S. Preston and D. V. Thiel, "Direction finding using a switched parasitic antenna array," *Antennas and Propagation Society Int. Symp*, vol. 2, pp. 1024–1027, July 1997.

[20] A. Cidronali, S. Maddio, S. G. Giorgetti, and G. Manes, "Analysis and performance of a smart antenna for 2.45-GHz single-anchor indoor positioning," *IEEE Trans. on Microwave Theory and Techniques*, vol. 58, no. 1, pp. 21–31, January 2010.

[21] K. Kim, T. K. Sarkar, M. C. Wicks, R. F. Recio, and M. S. Palma, "DOA estimation utilizing directive elements on a conformal surface," *Proc. of the 2003 IEEE Radar Conf*, pp. 91–96, May 2003.

[22] R. Sanudin, N. Noodin, A. El-Rayis, N. Haridas, A. Erdogan, and T. Arslan, "Analysis of DOA estimation for directional and isotropic antenna arrays," in *Loughborough Antennas and Propagation Conf. (LAPC)*, 2011, pp. 1–4.

[23] ——, "Capon-like DOA estimation algorithm for directional antenna arrays„" in *Loughborough Antennas and Propagation Conf. (LAPC)*, 2011, pp. 1–4.

[24] C. Chang, T. Cheng, and H. Lin, "Fast direction finding algorithm for circular array based on directional antenna," *Int. Workshop on Microwave and Millimeter Wave Circuits and System Technology (MMWCST)*, pp. 1–4, 2012.

[25] M. Pesavento and J. Bohme, "Direction of arrival estimation in uniform circular arrays composed of directional elements," *Sensor Array and Multichannel Signal Processing Workshop Proceedings*, pp. 503–507, August 2002.

[26] H. Gazzah and S. Marcos, "Cramer-Rao bounds for antenna array design," *IEEE Trans. on Signal Processing*, vol. 54, no. 1, January 2006.

[27] U. Baysal and R. L. Moses, "On the geometry of isotropic arrays," *IEEE Trans. on Signal Processing*, vol. 51, no. 6, pp. 1469–1478, June 2003.

[28] D. T. Vu, A. Renaux, R. Boyer, and S. Marcos, "A Cramer-Rao bounds based analysis of 3d antenna array geometries made from ULA branches," *Multidimensional Systems and Signal Processing*, vol. 24, no. 1, pp. 121–155, March 2013.

[29] C. Balanis and P. Ioannides, *Introduction to smart antennas*. Morgan & Claypool, 2007.

[30] F. Gross, *Smart antennas for wireless communications with MATLAB*. New York: McGraw-Hill, 2005.

[31] J. Liberti and T. Rappaport, *Smart antennas for wireless communications IS-95 and third generation CDMA applications*. New Jersey: Prentice Hall PTR, 1990.

[32] R. Schmidt, "Multiple emitter location and signal parameter estimation," *IEEE Trans. on Antennas and Propagation*, vol. 34, no. 3, March 1986.

[33] M. Wax and T. Kailath, "Detection of signals by information theoretic criteria," *IEEE Trans. on Acoustics, Speech and Signal Processing*, vol. 33, no. 2, pp. 387–392, April 1985.

[34] M. Landmann, M. Kaske, and R. Thoma, "Impact of incomplete and inaccurate data models on high resolution parameter estimation in multidimensional channel sounding," *IEEE Transactions on Antennas and Propagation*, vol. 60, no. 2, pp. 557–573, February 2012.

[35] M. Landmann, A. Richter, and R. Thoma, "DoA resolution limits in MIMO channel sounding," in *2004 IEEE International Symposium On Antennas and Propagation and USNC/URSI National Radio Science Meeting*, Monterey, CA, June 2004, pp. 20–26.

[36] F. Bellili, S. Affes, and A. Stephenne, "On the lower performance bounds for doa estimators from linearly-modulated signals," in *25th Biennial Symposium on Communications (QBSC)*, Kingston, Canada, May 2010, pp. 381–386.

[37] M. Gavish and A. Weiss, "Array geometry for ambiguity resolution in direction finding," *IEEE Trans. on Antennas and Propagation*, vol. 44, no. 6, June 1996.

[38] J. D. Kraus, *Antennas*. McGraw-Hill, 1988.

[39] P. Stoica and A. Nehorai, "MUSIC, maximum likelihood, and Cramer-Rao bound," *IEEE Trans. on Acoustics, Speech, and Signal Processing*, vol. 37, no. 5, May 1989.

[40] "FEKO user's manual suite 6.0," *EM Software & Systems-S.A. (Pty) Ltd.*, 2010.

[41] R. Sturdivant, "Balun designs for wireless... mixers, amplifiers and antennas," *Applied Microwave & Wireless*, Summer 1993.

[42] B. Climer, "Analysis of suspended microstrip taper baluns," *IEE Proceedings H, Microwaves, Antennas and Propagation*, vol. 135, no. 2, pp. 65–69, Apr 1988.

[43] K. Vinayagamoorthy, J. Coetzee, and D. Jayalath, "Microstrip to parallel strip balun as spiral antenna feed," in *2012 IEEE 75th Vehicular Technology Conference (VTC Spring)*, May 2012, pp. 1–5.

[44] P. Carro and J. de Mingo, "Analysis and synthesis of double-sided parallel-strip transitions," *IEEE Transactions on Microwave Theory and Techniques*, vol. 58, no. 2, pp. 372–380, February 2010.

[45] P. Carro, J. de Mingo, P. Garcia-Ducar, and C. Sanchez, "Synthesis of hecken-tapered microstrip to paralell-strip baluns for UHF frequency band," in *2011 IEEE MTT-S International Microwave Symposium Digest*, June 2011, pp. 1–4.

[46] S. Rizvi and R. Khan, "Klopfenstein tapered 2-18 GHz microstrip balun," in *2012 9th International Bhurban Conference on Applied Sciences and Technology (IBCAST)*, January 2012, pp. 359–362.

[47] R. Sefa and A. Maraj, "Analysis and design of microstrip to balanced stripline transitions," in *Proceedings of the 10th World Scientific and Engineering Academy and Society (WSEAS) International Conference on Telecommunications, Informatics, Electronics, and Signal Processing*, 2011, pp. 137–142.

Annex A: List of Acronyms

2D	Two-Dimensions
3D	Three-Dimensions
AOA	Angle of Arrival
ARV	Array Response Vector
CAF	Canadian Armed Forces
CBF	Classic Beamformer
CRLB	Cramer-Rao Lower-Bound
DF	Direction Finding
DOA	Direction of Arrival
DRDC	Defence Research and Development Canada
EM	Electromagnetic
FIM	Fisher Information Matrix
LOB	Line of Bearing
MoM	Method of Moments
MUSIC	Multiple Signal Classification
PCB	Printed Circuit Board
PVC	Polyvinyl Chloride
RF	Radio Frequency
RAM	Radiation Absorbent Material
RMC	Royal Military College of Canada
RMSE	Root-Mean-Square Error
SMA	Subminiature version A
SNR	Signal to Noise Ratio
TEM	Transverse Electromagnetic Mode
UCA	Uniform Circular Array
ULA	Uniform Linear Array
USRP	Universal Software Radio Peripheral
VNA	Vector Network Analyzer
XPD	Cross-Polarization Discrimination

This page intentionally left blank.

DOCUMENT CONTROL DATA

(Security markings for the title, abstract and indexing annotation must be entered when the document is Classified or Protected.)

1. ORIGINATOR (The name and address of the organization preparing the document. Organizations for whom the document was prepared, e.g. Centre sponsoring a contractor's report, or tasking agency, are entered in section 8.)

DRDC – Ottawa Research Centre
3701 Carling Avenue, Ottawa ON K1A 0Z4, Canada

2a. SECURITY MARKING (Overall security marking of the document, including supplemental markings if applicable.)

UNCLASSIFIED

2b. CONTROLLED GOODS

(NON-CONTROLLED GOODS)
DMC A
REVIEW: GCEC DECEMBER 2012

3. TITLE (The complete document title as indicated on the title page. Its classification should be indicated by the appropriate abbreviation (S, C or U) in parentheses after the title.)

Theory, design, and measurement of novel uniform circular antenna arrays for direction of arrival estimation

4. AUTHORS (Last name, followed by initials – ranks, titles, etc. not to be used.)

Jackson, B.; Liao, B.; Rajan, S.; Wang, S.

5. DATE OF PUBLICATION (Month and year of publication of document.)	6a. NO. OF PAGES (Total containing information. Include Annexes, Appendices, etc.)	6b. NO. OF REFS (Total cited in document.)
January 2015	78	47

7. DESCRIPTIVE NOTES (The category of the document, e.g. technical report, technical note or memorandum. If appropriate, enter the type of report, e.g. interim, progress, summary, annual or final. Give the inclusive dates when a specific reporting period is covered.)

Scientific Report

8. SPONSORING ACTIVITY (The name of the department project office or laboratory sponsoring the research and development – include address.)

DRDC – Ottawa Research Centre
3701 Carling Avenue, Ottawa ON K1A 0Z4, Canada

9a. PROJECT OR GRANT NO. (If appropriate, the applicable research and development project or grant number under which the document was written. Please specify whether project or grant.)	9b. CONTRACT NO. (If appropriate, the applicable number under which the document was written.)
15dr, 03dc	

10a. ORIGINATOR'S DOCUMENT NUMBER (The official document number by which the document is identified by the originating activity. This number must be unique to this document.)	10b. OTHER DOCUMENT NO(s). (Any other numbers which may be assigned this document either by the originator or by the sponsor.)
DRDC-RDDC-2015-R010	

11. DOCUMENT AVAILABILITY (Any limitations on further dissemination of the document, other than those imposed by security classification.)

Unlimited

12. DOCUMENT ANNOUNCEMENT (Any limitation to the bibliographic announcement of this document. This will normally correspond to the Document Availability (11). However, where further distribution (beyond the audience specified in (11)) is possible, a wider announcement audience may be selected.)

Unlimited distribution.

13. ABSTRACT (A brief and factual summary of the document. It may also appear elsewhere in the body of the document itself. It is highly desirable that the abstract of classified documents be unclassified. Each paragraph of the abstract shall begin with an indication of the security classification of the information in the paragraph (unless the document itself is unclassified) represented as (S), (C), or (U). It is not necessary to include here abstracts in both official languages unless the text is bilingual.)

The theory, design, fabrication, and measurement of new uniform circular arrays (UCAs) for direction of arrival (DOA) estimation is presented in this report. In particular, the effect of directional antenna elements in UCAs for DOA estimation is studied in detail. While the vast majority of previous work assumes isotropic antenna elements or omnidirectional dipoles, this work demonstrates that improved DOA estimation accuracy and increased bandwidth is achievable with appropriately-designed directional antennas. Simulation results in this report show improved DOA estimation accuracy and robustness using microstrip patch antennas as opposed to conventional dipoles. Additionally, it is shown that the bandwidth of a UCA for DOA estimation is limited only by the broadband characteristics of the directional antenna elements and not the electrical size of the array as is the case with omnidirectional antennas. Three novel UCAs were fabricated and tested: (1) a dipole UCA with integrated microstrip tapered baluns; (2) a narrow-spacing microstrip patch UCA; and (3) a wide-spacing microstrip patch UCA. Practical design aspects of all three arrays is detailed in this report and measurement results from an anechoic chamber are presented. This work shows that there are opportunities to improve direction finding performance through optimization of antenna array elements which could potentially improve Canadian Armed Forces direction finding and situational awareness capabilities.

14. KEYWORDS, DESCRIPTORS or IDENTIFIERS (Technically meaningful terms or short phrases that characterize a document and could be helpful in cataloguing the document. They should be selected so that no security classification is required. Identifiers, such as equipment model designation, trade name, military project code name, geographic location may also be included. If possible keywords should be selected from a published thesaurus. e.g. Thesaurus of Engineering and Scientific Terms (TEST) and that thesaurus identified. If it is not possible to select indexing terms which are Unclassified, the classification of each should be indicated as with the title.)

Direction of arrival (DOA) estimation, direction finding (DF), DOA using directional antennas, microstrip tapered balun, Array response vector (ARV), Cramer-Rao lower bound (CRLB), uniform circular array (UCA), microstrip antennas, antenna arrays

DRDC | RDDC

SCIENCE, TECHNOLOGY AND KNOWLEDGE FOR CANADA'S DEFENCE AND SECURITY | SCIENCE, TECHNOLOGIE ET SAVOIR POUR LA DÉFENSE ET LA SÉCURITÉ DU CANADA

www.drdc-rddc.gc.ca